MIT Open Access Articles

Positively-Coated Nanofiltration Membranes for Lithium Recovery from Battery Leachates and Salt-Lakes: Ion Transport Fundamentals and Module Performance

Positively-Coated Nanofiltration Membranes for Lithium Recovery from Battery Leachates and Salt-Lakes: Ion Transport Fundamentals and Module Performance

Zi Hao Foo, Suwei Liu, Lucy Kanias, Trent R. Lee, Samuel M. Heath, Yasuhiro Tomi, Tomotsugu Miyabe, Sinan Keten, Richard M. Lueptow,* and John H. Lienhard*

Membranes facilitate scalable and continuous lithium concentration from hypersaline salt lakes and battery leachates. Conventional nanofiltration (NF) membranes, however, exhibit poor monovalent selectivity in high-salinity environments due to weakened exclusion mechanisms. This study examines polyamide NF membranes coated with polyelectrolytes enriched with ammonium groups to maintain high monovalent cation selectivity in hypersaline conditions. Over 8000 ion rejection measurements are recorded using salt lake brines and battery leachates. The experiments exemplify the coated membrane's ability to reduce magnesium concentrations to 0.14% from salt lakes and elevate lithium purity to 98% from battery leachates, in a single filtration stage. The membrane's selectivity is retained after 12 weeks in acidic conditions. Molecular dynamics analyses reveal that the ammonium groups create an electrostatic barrier at low pH, selectively hindering multivalent cation transport. This is corroborated by the Coulombic attraction between cations and carboxylate groups, along with a repulsive barrier from ammonium groups. Despite a 14.7% increase in specific energy, a two-stage NF system using the coated membranes for lithium recovery significantly reduces permeate magnesium composition to 0.031% from Chilean salt lake brines. For NMC leachates, the coated membranes achieve permeate lithium purity exceeding 99.5%, yielding enhanced permeate quality with minor increases in energy demands.

1. Introduction

Continuous development of energy storage technologies, such as batteries and capacitors, is essential for advancing electric mobility, increasing the reliability of clean energy solutions, and fostering sustainable power generation.[1,2] Economic forecasts predict a significant annual rise in lithium-ion battery demand, with estimates of up to 30% year-on-year growth across the transportation, portable electronics, and renewable energy sectors.[3,4] Such an increase could multiply the demand for battery-grade lithium by forty-fold by 2040, highlighting the critical need for sustainable, scalable, and cost-effective lithium extraction and production methods.[4,5]

The global lithium demand is presently satisfied from two principal channels: 1) primary sources, which involve mining spodumene ores and extracting from salt lake brines; and 2) secondary sources, encompassing the recycling of spent batteries and capacitors.[6,8–10] However, extracting

Z. H. Foo, T. R. Lee, S. M. Heath, J. H. Lienhard
Department of Mechanical Engineering
Massachusetts Institute of Technology
Cambridge, MA 02139, USA
E-mail: lienhard@mit.edu
Z. H. Foo
Center for Computational Science and Engineering
Massachusetts Institute of Technology
Cambridge, MA 02139, USA

S. Liu, S. Keten, R. M. Lueptow
Department of Mechanical Engineering
Northwestern University
Evanston, IL 60208, USA
E-mail: r-lueptow@northwestern.edu
L. Kanias
Department of Chemical Engineering
Massachusetts Institute of Technology
Cambridge, MA 02139, USA
Y. Tomi, T. Miyabe
Membrane Division
Nitto Denko Corporation
Shiga 5250042, Japan
S. Keten
Department of Civil and Environmental Engineering
Northwestern University
Evanston, IL 60208, USA
R. M. Lueptow
Department of Chemical and Biological Engineering
Northwestern University
Evanston, IL 60208, USA

**ADVANCED
SCIENCE NEWS**

www.advancedsciencenews.com

**ADVANCED
FUNCTIONAL
MATERIALS**

www.afm-journal.de

lithium from primary sources using commercial methods, such as the evaporation of salt lake brines, requires approximately 800 cubic meters of freshwater for every metric ton of lithium carbonate produced.[4,11] Such practices aggravate water scarcity in the world's most arid regions and contribute to aquifer contamination and wetland degradation, due to the extensive deployment of evaporation ponds.[4,12] Moreover, the protracted production cycles characteristic of evaporation ponds constitute a major bottleneck in lithium production, leading to a market supply that is economically inelastic and insufficiently responsive to demand fluctuations.[4,13]

On the other hand, the compact configuration of modern lithium-ion batteries, comprising electrodes, casings, and electrolytes, necessitates a comprehensive array of processes for effective recycling.[3,14,15] The current recycling paradigm involves a sequence of treatments–pyrolysis, physical and magnetic separation, followed by hydrometallurgical extraction through acid leaching.[3,16] This sequence results in an effluent enriched with critical metals such as lithium (Li), cobalt (Co), manganese (Mn), and nickel (Ni).[17,18] Post acid leaching, the effluent is typically treated using ion exchange columns that employ resins to selectively capture or adsorb specific ions.[7,10] Despite its efficacy, this heavy reliance on ion exchange technology poses considerable technical and economic challenges due to the high energy consumption and significant acid waste production during resin regeneration.[3,18] Consequently, only a minor fraction, less than 6%, of spent lithium-ion batteries are currently recycled worldwide, with the majority being relegated to landfills.[3] Such disposal raises environmental concerns, including the potential for toxic gas evolution or heavy metals leaching into underground aquifers.[3,14,16]

Therefore, the innovation of selective technologies that extract critical metals from salt lakes and battery leachates with a minimal number of steps under ambient condition is of paramount importance.[19,20] Recent technological advancements encompass solvent-driven methods employing ionic liquids, deep eutectic solvents, and fractional crystallization;[21–24] electrochemical approaches such as capacitive deionization (CDI) and electrochemically switched ion exchange (ESIX);[9,25] and membrane technologies like nanofiltration (NF) and electrodialysis (ED).[26–29] Due to its high energy efficiency, ease of scalability and cost-effectiveness, NF continues to garner considerable research interest as a key unit operation for lithium recovery.[19,26,27,30–33] In the context of salt-lake lithium extraction, as illustrated in **Figure 1A**, the application of a highly selective NF process can efficiently eliminate multivalent cations like Mg^{2+} and Ca^{2+}. These multivalent cations have solubility products similar to Li_2CO_3 and tend to co-precipitate, and their elimination improves the purity of the recovered lithium from downstream direct lithium extraction processes.[34] Moreover, NF facilitates the concentration of salt-lake brine without resorting to evaporation ponds, offering a continuous unit operation to alleviate the supply inelasticity of existing extraction methods. In the treatment of battery leachates, as depicted in Figure 1B, a selective NF process facilitates the separation of monovalent lithium cations from a mixture of multivalent transition metal cations. This enhances the yield of recovered lithium and minimizes acid production by reducing the number of ion exchange column stages required.[14,17]
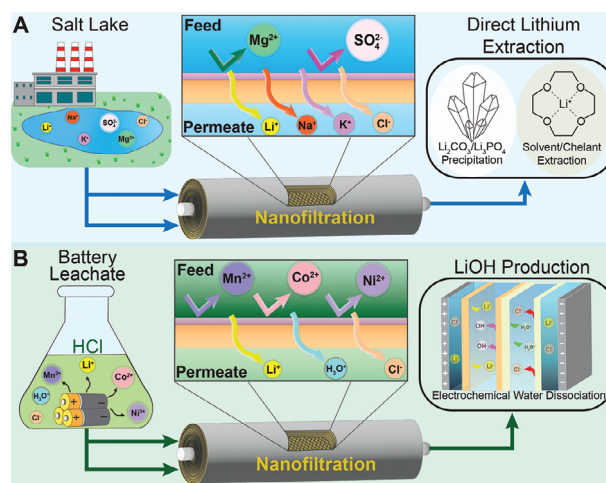

Figure 1. Schematic diagram illustrating nanofiltration (NF) for lithium extraction from salt lakes and battery leachates. A) Salt lake brine comprises a high concentration of Mg^{2+} ions that attenuate the extraction efficiency of precipitation, adsorption and chelation-based direct lithium extraction technology.[6] NF selectively eliminates Mg^{2+} while concentrating Li^+ in the permeate stream. B) Battery leachates comprise high concentrations of Li^+, Mn^{2+}, Co^{2+}, and Ni^{2+} ions.[7] NF produces a concentrated Li^+ permeate stream that is amenable for LiOH production.

Conventional NF membranes are composed of a polyamide active layer on a polysulfone support, cross-linked through a condensation reaction between piperazine and trimesoyl chloride. Ion fractionation in NF relies on steric, dielectric, and Donnan exclusion mechanisms;[35,36] the latter originates from the electrostatic potential conferred by residual negatively-charged carboxylate and positively-charged ammonium functional groups within the polyamide layer.[37] This electrostatic potential varies with solution pH, becoming positive under low pH and negative at high pH, as governed by the ionic equilibrium affecting the concentration of carboxylate (COO^-) and ammonium (NH_2^+) functional groups within the polyamide layer.[38] With dilute binary Li^+-Mg^{2+} solutions, commercial polyamide NF membranes can achieve a significant increase in monovalent cation selectivity—an order of magnitude—by amplifying the Donnan potential at low solution pH.[39] With salt-lake brines or battery leachates that have hypersaline concentrations exceeding 250 g L^{-1}, however, this selectivity enhancement is nullified by the attenuated exclusion efficacy in the membrane's active layer.[40–42]

To sustain high monovalent cation selectivity in hypersaline conditions, we introduce and characterize high-permeability polyelectrolyte surface coatings endowed with a high density of NH_2^+ functional groups to facilitate lithium recovery from salt lakes and battery leachates. We evaluate the selectivity performance of both uncoated and coated polyamide membranes through bench-scale experiments with brines representative of Chilean and Chinese salt lakes, and leachates from NMC and LMO battery cathodes, compiling an original dataset of over 8000 ion rejection measurements. When juxtaposed with membranes reported in existing literature, our measurements suggest that the coated NF membrane is amongst the most competitive options for lithium concentration. We conduct complementary ion partitioning studies to elucidate the mechanisms
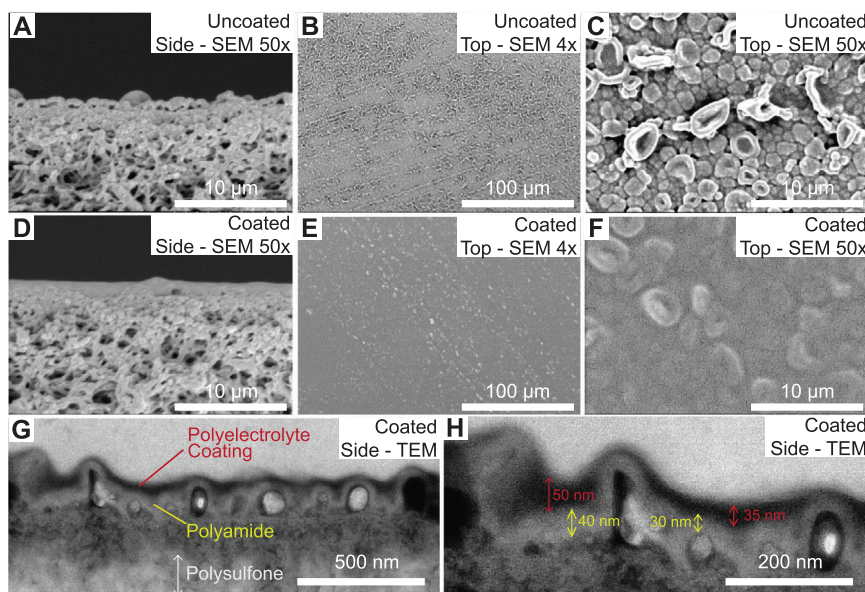
Figure 2. Scanning electron microscopy (SEM) is utilized to analyze the morphology of the uncoated nanofiltration membrane, showcasing the cross-section at (A) 50x magnification and the surface at (B) 4× and (C) 50x magnifications. Additionally, the positively-coated membrane is similarly examined using SEM, highlighting its cross-section at (D) 50x magnification and surface at (E) 4× and (F) 50x magnifications. G, H) Further observations of the positively-coated membrane's cross-section are performed using transmission electron microscopy. The higher resolution microscopy illustrates the color-contrasted layers, including the polyelectrolyte surface coating, the polyamide active layer, and the polysulfone support layer.

underpinning the observed enhancement in ion selectivity conferred by the coatings. Our molecular dynamics (MD) simulations uncover Coulombic energy barriers between the NH_2^+ functional groups and cations, which disproportionately impedes the partitioning of multivalent cations over lithium. This molecular-level understanding, corroborated by empirical measurements on the zeta potential, pore sizes, and ion partitioning rates, suggests that charge-based exclusion of multivalent cations is principally responsible for the observed selectivity enhancements. Lastly, we perform module-scale computational analysis using a coated spiral-wound membrane to quantify the potential enhancements in thermodynamic efficiency achievable in industrial NF treatment processes employing Donnan-enhanced NF membranes.

2. Results and Discussion

2.1. Polyelectrolyte Surface Coating Amplifies Donnan Exclusion of Multivalent Cations

In this work, we develop two types of nanofiltration (NF) membranes that recover monovalent cations like lithium from salt-lake brines and battery leachates, as detailed in Section Chemicals and Materials. The first variant, referred to as the uncoated NF membrane, consists of a conventional semi-aromatic polyamide active layer formed through interfacial polymerization of piperazine and trimesoyl chloride on a polysulfone support structure.[32,43] The second variant, termed the coated NF membrane, is created by covalently condensing a highly cross-linked, acid-resistant polyelectrolyte coating onto the polyamide layer of a conventional NF membrane.[44–46] The polyelectrolyte coating, characterized by a high density of positively-charged ammonium

(NH_2^+) functional groups, is designed specifically to enhance the charge-based exclusion of multivalent cations.[47–50] Additional details on the chemical structure are provided in the Supporting Information.

Scanning electron microscopy (SEM) is employed to examine the cross-sectional and surface characteristics of these membranes. The findings for the uncoated membrane are presented in **Figure** 2A–C, while the observations for the coated membrane are illustrated in Figure 2D–F. The cross-sectional view of the conventional (uncoated) NF membrane, as depicted in Figure 2A, reveals a thin and dense polyamide active layer that is polymerized atop a porous polysulfone support layer. Similarly, Figure 2D exhibits the successful deposition of a highly cross-linked, dense polyelectrolyte surface coating over the polyamide active layer. Higher resolution cross-sectional analysis of the coated membrane is conducted with transmission electron microscopy (TEM), as depicted in Figure 2G–H. The TEM images confirm the successful deposition of the polyamide and polyelectrolyte layers, and reveal that the thickness of the polyamide and polyelectrolyte layers ranges from 30–40 nm and 35–50 nm, respectively. Further, Figure 2B–C reveals a ridge-and-valley surface morphology for the polyamide layer in the conventional uncoated membrane, which is consistent with prior characterization of similar semi-aromatic NF membranes.[51,52] The addition of the polyelectrolyte surface coating to the polyamide layer, as shown in Figure 2E,F, leads to a reduction in surface roughness of the composite membrane, aligning with outcomes previously observed for similar surface coatings.[32,53,54]

The penetration depth of Fourier transform infrared spectroscopy (FTIR), which typically extends up to 5 µm, facilitates the analysis of functional groups within the thin-film polyamide (40 nm) and polyelectrolyte (50 nm) layers.[55] The polyester

**ADVANCED
SCIENCE NEWS**

www.advancedsciencenews.com

**ADVANCED
FUNCTIONAL
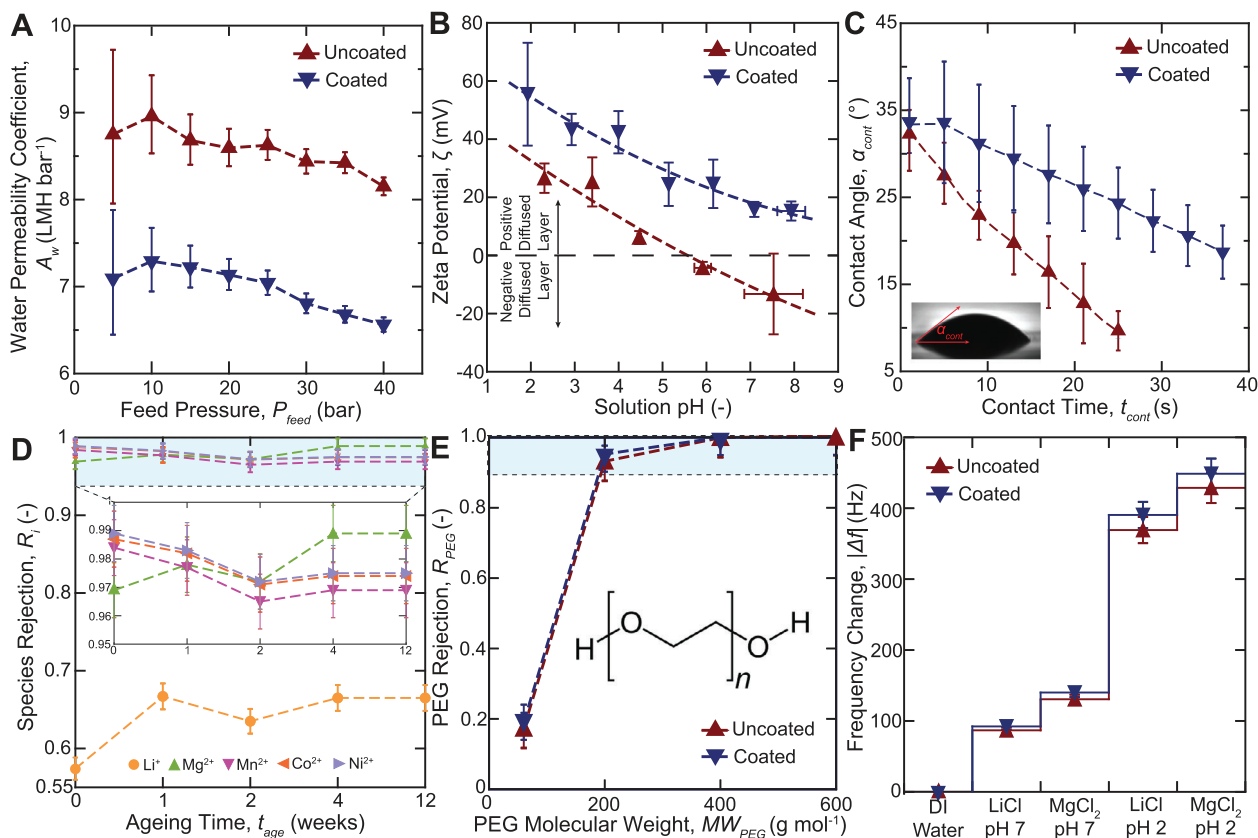MATERIALS**

www.afm-journal.de

Figure 3. A) Relationship between the membrane's water permeability coefficient and the applied feed pressure, indicating a 21% reduction in solvent permeability due to the hydraulic resistance of the polyelectrolyte surface coating. B) Zeta potential measurements of the membrane's diffuse layer correlated with solution pH, revealing a consistently positive zeta potential in coated membranes across the spectrum of tested pH. C) Comparative contact angle data for uncoated and coated membranes, demonstrating that the polyelectrolyte coating does not diminish the hydrophilicity of the active layer. D) Ion rejection performance of the coated membrane in ageing experiments. The coated membrane maintains high multivalent ion rejections in acidic conditions over a 12-week period. E) Species rejection as a function of the molecular weight for the molecular weight cut-off experiments with polyethylene glycol (PEG), suggesting that the addition of the polyelectrolyte coating does not impact size-based exclusion effects. F) Changes in the fundamental resonance frequency derived from quartz crystal microbalance with dissipation monitoring (QCM-D) measurements. Solutions with lower pH and multivalent cation register greater frequency change for both uncoated and coated membranes.

backings of both uncoated and coated membranes are carefully removed, and the infrared spectra of the polyamide and polyelectrolyte layers are captured with FTIR, as detailed in Figure S16 (Supporting Information). The FTIR spectra of the uncoated polyamide layer reveal distinct features: a sharp transmittance peak at 1730 cm^{-1} for C=O stretching in the carboxylate functional group, a sharp peak between 2800 and 2900 cm^{-1} for C-H stretching in the aliphatic structure, and a broad peak from 3200 to 3600 cm^{-1} indicating primary and secondary N-H stretching in the ammonium functional group, all of which are consistent with previous characterizations reported in the literature.[31,32,56] On the other hand, the polyelectrolyte-coated polyamide layer exhibits similar peaks at the corresponding wavenumbers, with a significantly deeper transmittance well for N-H stretching and a slightly shallower well for C=O stretching. The FTIR results suggest that the incorporation of the polyelectrolyte coating increases the density of NH$_2^+$ functional groups and slightly decreases the density of COO$^-$ functional groups within the coated membrane, across the range of the four tested pH values.

The characterizations of the active layers in both uncoated and coated membranes are consolidated in **Figure** 3A–F. Figure 3A highlights the impact of the addition of the polyelectrolyte coating on the apparent water permeability of the NF membrane. Due to the hydraulic resistance imparted by the polyelectrolyte coating, the membrane's water permeability coefficient shows a decrease ranging from 12.5 to 18.7%, ascertained using ultrapure water feed solutions at pressures between 5 to 40 bar. Despite the doubling of the active layer (polyamide and polyelectrolyte) thickness, the membrane's water permeability coefficient decreases less than proportionally and remains sufficiently high to facilitate efficient lithium concentration processes.[50] The zeta potential for both the uncoated and coated membranes is calculated using the Smoluchowski equation, as depicted in Figure 3B, quantifying the electric potential of the slip plane in the electric double layer.[57] The conventional uncoated membrane displays an isoelectric point at around a pH of 5.5, in contrast to the coated membrane, which shows a consistently net positive active layer throughout a pH range of 2 to 8. This observation aligns with our FTIR results, where the addition of a polyelectrolyte layer

**ADVANCED
SCIENCE NEWS**

www.advancedsciencenews.com

**ADVANCED
FUNCTIONAL
MATERIALS**

www.afm-journal.de

enriched with positively-charged NH_2^+ functional groups resulted in a deeper N-H transmittance well and a positive zeta potential, persisting even in alkaline solutions. Moreover, the zeta potential of both uncoated and coated membranes increases as the solution pH decreases, which is attributable to the protonation of the uncrosslinked NH groups in the polyamide layer to yield more positively-charged NH_2^+ functional groups,[38] as governed by ionic equilibrium.

The wettability analysis for both uncoated and coated membranes is presented in Figure 3C. The advancing contact angle measurements indicate that polyelectrolyte addition does not diminish the apparent hydrophilicity of the membrane's surface, maintaining a three-phase contact angle of 34°. The difference in the rate of decline in the advancing contact angle measurements, however, suggests a lower surface permeability in the polyelectrolyte-coated membrane, corroborating the findings from the water permeability experiments.[58] The acid resistance of the coated membrane is evaluated by submerging it in a 0.5 M HCl solution for up to 12 weeks. As shown in Figure 3D, the rejections of Li^+ and Mg^{2+} are calculated from Chilean salt-lake brine experiments while the rejections of Co^{2+}, Mn^{2+}, and Ni^{2+} are calculated with NMC battery leachates. The ageing experiment results indicate that the ion rejection capability of the coated membrane is sustained under acidic conditions over a 12-week period, suggesting that it may be tolerant to acid pre-treated salt-lake brines and battery leachates.

In the subsequent salt-lake brine and battery leachate experiments, we observed no flux decline or deposition of inorganic or organic fouling on the membrane surface, with saturation indices of ions below unity. While our study focused on the membrane's acid stability over 12 weeks in HCl, we recognize the critical impact of fouling on the long-term performance and economic viability of nanofiltration processes.[59] Inorganic fouling, caused by mineral scale deposition, and organic fouling, due to the accumulation of biofilms and organic materials, can significantly affect membrane functionality.[60–62] Given the varied compositions of salt-lakes and battery leachates, it is challenging to generalize fouling behavior, making it essential to conduct systematic investigations under representative conditions.[59,61] Future studies should prioritize exploring fouling mechanisms and mitigation strategies to ensure the sustained high performance and practical application of nanofiltration membranes.[63]

Figure 3E and Table S14 (Supporting Information) present the solute rejection measured in relation to the molecular weight during coupon-scale experiments with uncharged polyethylene glycol (PEG), across a solution pH range of 2 to 7. The invariability in PEG rejection observed with both uncoated and coated membranes across the pH range suggests that size-based exclusion is not the primary mechanism of the differences in lithium selectivity observed in subsequent experiments with salt-lake and battery leachate solutions.[64,65] The calculated pore size distributions are similar for both uncoated and coated membranes across the tested pH levels, with average pore radii of 0.305 ± 0.085, 0.310 ± 0.095, and 0.310 ± 0.092 nm for uncoated membranes at pH 7, 4, and 2 respectively, and 0.306 ± 0.093, 0.305 ± 0.098, and 0.301 ± 0.098 nm for coated membranes under the same conditions. According to classical nanofiltration pore-flow model, therefore, the observed differences in ion selectivity with the coating are unlikely due to size-based exclusion mechanisms.[35]

Furthermore, Figure 3F displays the shifts in fundamental resonance frequency of membrane-coated gold sensors, as measured by quartz crystal microbalance with dissipation monitoring (QCM-D). According to QCM-D literature, changes in the fundamental resonance frequency reflect mass alterations in the membrane's active layer on the sensor. A positive frequency shift signals a decrease in mass based on the Sauerbrey equation, indicating a change in the water or ion partitioning behavior in the active layer.[66,67] Our QCM-D results reveal a more significant frequency shift at lower solution pH levels and with $MgCl_2$ as compared to LiCl, with a more pronounced change registered with the polyelectrolyte-coated membrane. The QCM-D results, when integrated with the molecular weight cut-off, membrane pore size, FTIR and zeta potential measurements, suggest that the charge-based partitioning effects have been enhanced, thereby favoring the Donnan exclusion of multivalent cations such as Mg^{2+} over monovalent cations like Li^+.

2.2. Positively-Coated Nanofiltration Enhances Lithium Purity from Salt-Lakes and Battery Leachates

Bench-scale experiments with 8.0 cm by 3.0 cm coupons are conducted employing both uncoated and coated NF membranes. The influence of the polyelectrolyte layer and various process conditions on the apparent selectivity for monovalent ions in the NF membrane is evaluated based on an original dataset of over 8000 ion rejection measurements. These experiments encompass process conditions spanning solution pH from 0.5 to 7 and feed salinities between 10 to 250 g L^{-1}, across two salt-lake brine and two battery leachate compositions. The complete data on ion rejections are fully compiled in Tables S6–S13 (Supporting Information), while detailed plots for all dissolved ions are presented in Figures S5–S13 (Supporting Information).

Figure 4A,D illustrates the ion rejection of Li^+ and Mg^{2+}, and Li^+ and Co^{2+} with the coated membrane, from the Chilean salt-lake brine and NMC battery leachate, respectively. The measured ion rejection, which is illustrated with solid markers, is evaluated with respect to the solution pH and the driving water flux, while the solid curves denote the predictions from the calibrated Donnan-steric pore model with dielectric exclusion (DSPM-DE). The measured ion rejections increase with the water flux, tending toward an asymptotic value at the upper limit.[35] For the Chilean and Chinese salt-lakes and the NMC and LMO battery leachates, the coated membrane consistently demonstrates superior rejection of multivalent cations (e.g., Mg^{2+}, Mn^{2+}, Ni^{2+}, and Co^{2+}) compared to monovalent ions (e.g., Li^+, Na^+, and K^+), with the disparity in ion permeation rates widening at lower solution pH levels. For instance, with Chilean salt-lake brines, Li^+ permeation decreases from 65.6 to 42.3%, while Mg^{2+} permeation decreases by an order of magnitude from 8.8 to 0.9%, when the solution pH decreases from 7 to 2. Similarly, over the pH interval between 4 to 0.5 with NMC battery leachates, Li^+ permeation decreases from 96.0 to 53.1%, and Co^{2+} rejection decreases from 3.9 to 1.1% with the coated membrane. This reduction in both monovalent and divalent cation permeation rates over the pH interval correlates with the observed decrease in ion partitioning and an increase in NH_2^+ functional group density, as presented in

**ADVANCED
SCIENCE NEWS**

www.advancedsciencenews.com

**ADVANCED
FUNCTIONAL
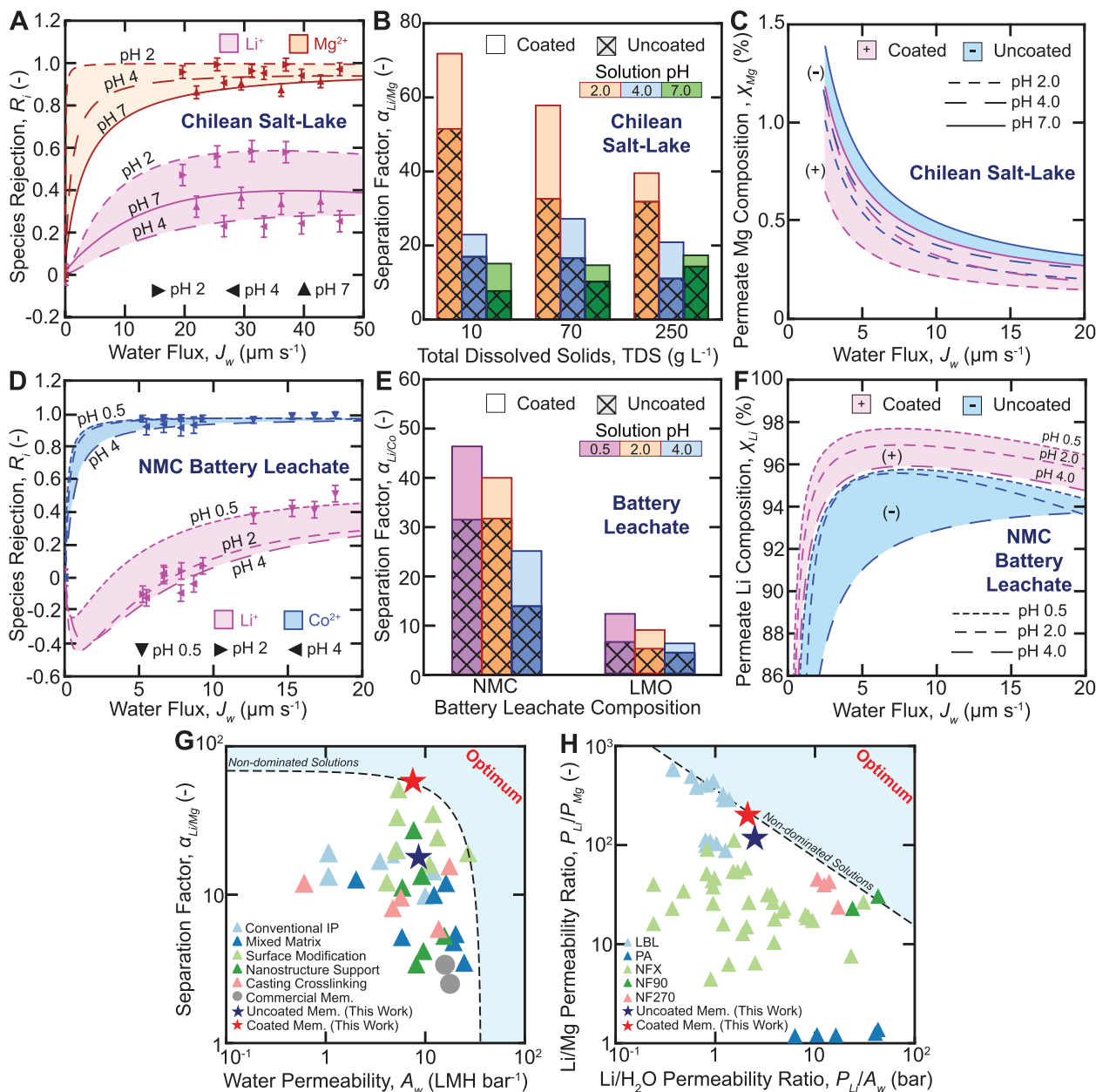MATERIALS**

www.afm-journal.de

Figure 4. A) Species rejection in relation to solution pH and transmembrane flux for the coated nanofiltration (NF) membrane with Chilean salt-lake brines. B) The Li/Mg separation factor for both uncoated and coated NF membranes is plotted against the total dissolved solids concentration and pH of the Chilean salt-lake brine, demonstrating enhanced lithium selectivity with coated membranes across all tested solution concentrations and pH levels. C) Measurement of residual Mg concentration in the permeate after a single-pass NF treatment of Chilean salt-lake brines using uncoated and coated membranes, depicted as a function of solution pH and transmembrane flux. D) Species rejection against solution pH and transmembrane flux for the coated NF membrane to treat NMC battery leachates. E) The Li/Co separation factor of uncoated and coated NF membranes in relation to leachate composition and pH. F) The purity of lithium in the permeate from a single-pass NF treatment of NMC battery leachates using both uncoated and coated membranes, shown as a function of solution pH and transmembrane flux. Robeson plots illustrating the trade-off between (G) separation factor and solvent permeability coefficient,[49] and (H) Li/Mg permeability and Li/H$_2$O permeability.[68] The solid markers represent measurements for a variety of NF membranes, as compiled by Wang et al.[49] and Wang et al.,[68] respectively. The Robeson plots indicate that the positively-coated NF membrane is a non-dominated solution to the multi-objective optimization problem.

**ADVANCED
SCIENCE NEWS**

www.advancedsciencenews.com

**ADVANCED
FUNCTIONAL
MATERIALS**

www.afm-journal.de

Section 2.1, suggesting that Donnan exclusion played a primary role in enhancing the membrane's monovalent selectivity.

Figure 4B shows the effect of feed salinity and solution pH on the Li/Mg separation factor ($\alpha_{Li/Mg}$) with Chilean salt-lake brines, where clear and hatched bars indicate the selectivity of the coated and uncoated membranes, respectively. The addition of the polyelectrolyte coating leads to an increase in $\alpha_{Li/Mg}$ values by as much as 70%, especially under acidic conditions at pH 2. This notable enhancement in monovalent selectivity, most pronounced in coated NF membranes with the highest density of NH_2^+ functional groups at pH 2, further corroborates that charge-screening exclusion mechanisms are likely responsible for the significantly improved rejection of Mg^{2+}. Additionally, the monovalent selectivity decreases for both uncoated and coated membranes as the salinity of the Chilean brine rises from 10 to 250 g L^{-1}, a trend seen in prior publications involving hypersaline brines.[39,69] The decline in selectivity has been attributed to the reduced efficacy of the Donnan exclusion mechanism, occurring when the ionic strength of the feed solution approaches the molar charge density of the membrane's active layer.[36,70] Despite this, the coated NF membrane retains a high separation factor of approximately 40, which is 5 to 8 times greater than that of standard commercial polyamide NF membranes.[39]

Figure 4C illustrates the composition of residual Mg^{2+} (χ_{Mg}) in the permeate stream, detailing its variation with water flux and solution pH following a single stage of NF treatment with either the coated or uncoated membrane. The Mg^{2+} content in the permeate is expressed as a percentage of total cationic species to evaluate the membrane's effectiveness in concentrating salt-lake brines for downstream direct lithium extraction (DLE) processes.[29,34] To avoid clutter, solid markers are omitted (see Figures S5 to S13, Supporting Information for individual ion rejection plots). Due to the enhanced rejection of multivalent cations, the Mg^{2+} concentration in the permeate decreases as the driving water flux increases to 20 μm s^{-1}, which is consistent with the findings from Figure 4A. Similarly, the coated NF membranes consistently demonstrate reduced concentrations of residual Mg^{2+}, leveraging the enhanced Li/Mg separation factors afforded by the polyelectrolyte coating. For instance, the introduction of the polyelectrolyte coating further lowers the residual Mg^{2+} concentration by up to 42%, reducing χ_{Mg} from 0.20% to 0.14% and from 0.32% to 0.26% at pH levels of 2 and 7, respectively.

The impact of the battery leachate composition and the solution pH on the Li/Co separation factor ($\alpha_{Li/Co}$) is illustrated for both uncoated and coated membranes in Figure 4E. Consistent with the salt-lake brine experiments, the polyelectrolyte coating enhances the monovalent selectivity by up to 44% at a pH of 0.5, registering $\alpha_{Li/Co}$ of 46.8 and 13.1 with NMC and LMO leachates, respectively. Likewise, the greatest enhancements in monovalent selectivity are observed at low solution pH and with the coated membrane, circumstances that result in the highest molar density of positively-charged NH_2^+ functional groups. The permeate Li^+ composition (χ_{Li}) is illustrated in Figure 4F for the uncoated and coated membranes, as a function of the solution pH and the transmembrane water flux with NMC leachates. The incorporation of the polyelectrolyte coating leads to an average increase in the χ_{Li} by 3%, rising from a permeate Li^+ purity of 94.8% to 97.9%, using battery leachates with pH levels of 0.5 with

one NF treatment stage. In essence, by correlating the molecular properties of the charged functional groups to the observed separation performance with salt-lake brines and battery leachates, our experiments demonstrate that the integration of a polyelectrolyte surface coating enhances Donnan exclusion, increasing the monovalent selectivity by as much as 44%. Consequently, Donnan-enhanced nanofiltration can produce post-treated salt-lake brines with a residual Mg^{2+} concentration of only 0.14% and post-treated battery leachates with a Li^+ purity of 98%, all with a single-stage NF process.

Lastly, we juxtapose the selectivity and permeability performance of the uncoated and coated NF membranes against lab-scale and commercially available membranes reported in the literature. Nanofiltration membranes are inherently constrained by a trade-off between permeability and selectivity, where the ideal membrane would exhibit high permeability to enable high-flux recovery of the target cation(s), along with high selectivity to ensure the production of high purity permeate streams.[35,47] Figure 4G and H depict two standard analytical approaches to this dual-objective optimization in nanofiltration, with the optimal membrane scenario represented in the upper-right quadrant of each plot.[49,68,71] The selectivity and permeability metrics are evaluated with binary cation solutions, based on literature conventions.[49,68] The Pareto front, indicated by dashed lines, represents the optimal balance between permeability and selectivity currently achievable based on the multi-objective optimization in this paper. The solid markers represent measurements for a variety of NF membranes, as compiled by Wang et al.[49] and Wang et al.[68] The introduction of the polyelectrolyte coating, as shown in Figure 4G,H, significantly improves the Li/Mg separation factor and permeability ratio, while only marginally reducing water permeability and the Li/H_2O permeability ratio. Notably, unlike many other membranes depicted in the trade-off plots, this enhancement in selectivity is achieved with a membrane that is amenable to end-to-end rolling manufacturing and is commercially available as a spiral-wound module. When compared with the range of membranes documented by Wang et al.[49] and Wang et al.,[68] the performance of the polyelectrolyte-coated membrane appears to align with the Pareto front in these analytical plots, suggesting it is amongst the most competitive options for lithium recovery.

2.3. Molecular Dynamics Reveals Ion-Functional Group Interactions Enhance Membrane Selectivity

To provide molecular level insights into the interactions between NH_2^+ and COO^- functional groups in the membrane and feed ions in binary $LiCl/MgCl_2$ solutions, we conduct molecular dynamics (MD) analyses for feed solutions with pH values of 2 and 7. Although salt-lake brines contain both Cl^- and SO_4^{2-}, we only consider Cl^- because current MD models for sulfate result in computational problems where sulfates cluster pre-maturely in aqueous solutions.[72–74] At feed pH 2, the membrane's active layer is positively charged with only NH_2^+ functional groups present, and at pH 7 the active layer has a net negative charge with both NH_2^+ and COO^- groups present.[38] The NH_2^+ groups are distributed through the volume of the active layer, while the COO^- groups are concentrated near the membrane feed surface,
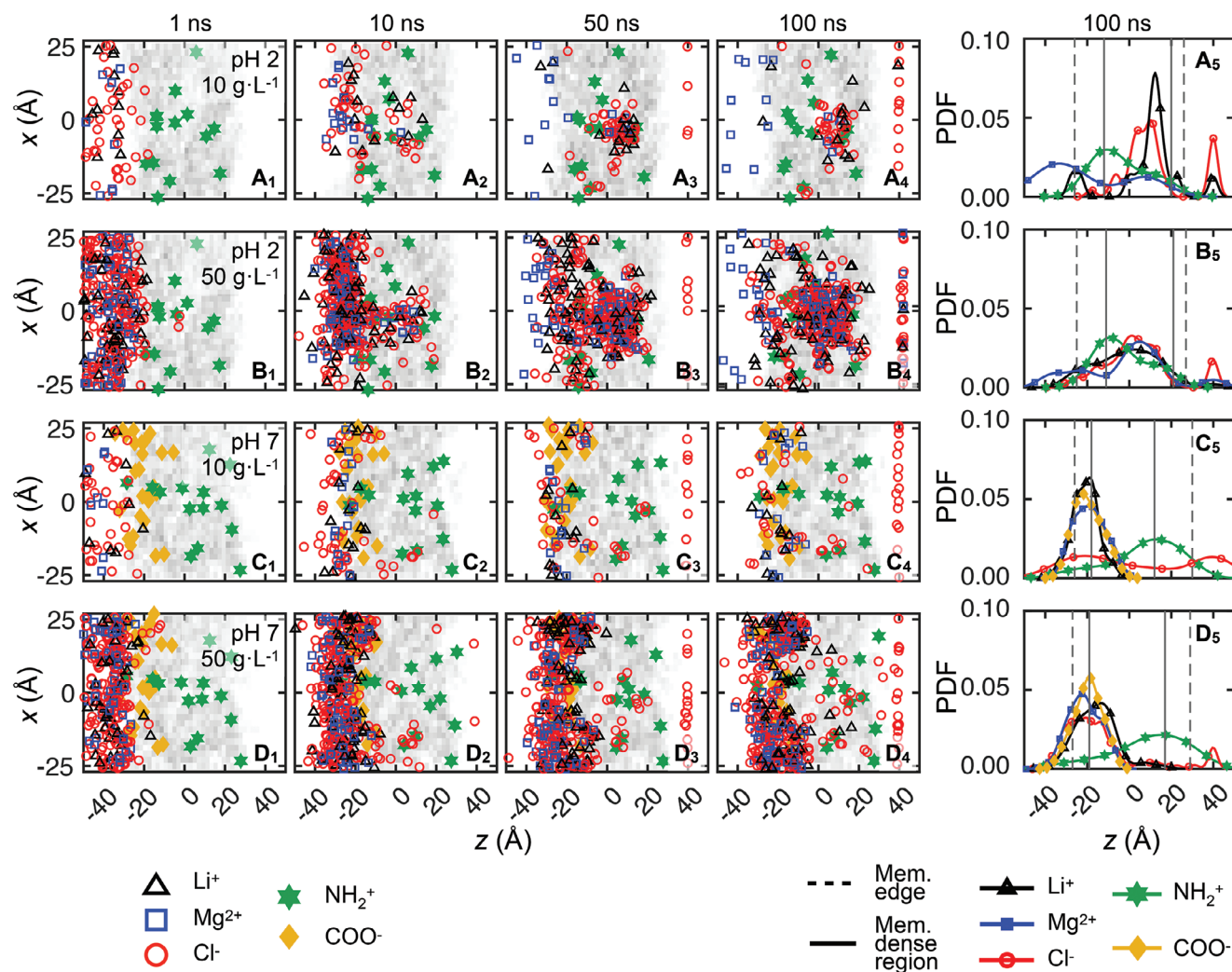
**ADVANCED
SCIENCE NEWS**

www.advancedsciencenews.com

**ADVANCED
FUNCTIONAL
MATERIALS**

www.afm-journal.de

Figure 5. Feed ion locations in the *xz*-plane across three trials for (A) pH 2 with 10 g L^{-1} TDS, (B) pH 2 with 50 g L^{-1} TDS, (C) pH 7 with 10 g L^{-1} TDS, and (D) pH 7 with 50 g L^{-1} TDS at (1) 1 ns, (2) 10 ns, (3) 50 ns, and (4) 100 ns. Gray areas indicate the local membrane density, where the darker gray implies higher density. (5) The probability density function of feed ions and membrane functional groups (COO$^-$, NH$_2^+$) in the *z*-direction at 100 ns. Dashed lines mark the edge-to-edge boundaries of the membrane model, and solid lines bound the densest regions of the membrane. For all feed solutions, LiCl and MgCl$_2$, share have the same molarity.

consistent with experimental results for charge distributions in polyamide membranes.[38,75] A detailed account of the simulation setup, assumptions and solution algorithm for MD appears in Section S4.3 (Supporting Information).

For both pH levels, the membrane system is simulated with two different concentrations. The dilute feed solution is 10 g L^{-1} TDS, corresponding to 5 Li$^+$, 5 Mg^{2+}, and 15 Cl$^-$ ions in the simulated system; the concentrated feed solution is 50 g L^{-1} TDS, corresponding to 25 Li$^+$, 25 Mg^{2+}, and 75 Cl$^-$ ions. The solution pH and concentration of the feed solutions are chosen to model the experimental conditions, as reported in the preceding sections. In all cases, we perform three simulations with all ions starting on the feed side of the membrane and tracking the progress of the ion ensembles through the membrane for 100 ns using the NAMD simulation package[76] at 300 K. To accelerate the sampling of ion passage in the limited duration for the MD simulations that is computationally feasible, we apply an external

body force to each feed ion in $+z$-direction, which is normal to the membrane surface (*xy*-plane), in order to accelerate the solute ion movement through the membrane. Videos illustrating the transport of ions across the membrane, as influenced by solution pH and concentration, are available in the Supporting Information.

To evaluate ion permeation at the nanoscale, we show the locations of all feed ions, combined across all three trials, in the *xz*-plane at four distinct time instances in **Figure 5A–D**. Note that the simulation domain is non-periodic in the *z*-direction and periodic in the *x*- and *y*-directions. Hence, Figure 5A–D depict the *x*-, *z*-locations of ions and charged functional groups through the 50 Å depth of the periodic domain in the *y*-direction. In order to better visualize the ion locations for ions permeating completely through the membrane, we reset the *z*-locations for any ions with $z > 40$ Å to $z = 40$ Å. The gray shading in the first four columns indicates the local density of membrane model with darker gray corresponding to higher density. The last column in Figure 5 shows

**ADVANCED
SCIENCE NEWS**

www.advancedsciencenews.com

**ADVANCED
FUNCTIONAL
MATERIALS**

www.afm-journal.de

the probability density function (PDF) of feed ion and membrane functional group z-locations at 100 ns.

First, we consider membrane systems simulated with a dilute feed at low pH, shown in Figure 5A. Here, Cl^- exhibits faster transport behavior compared to cations even at the start of the simulation (1 ns), where a few Cl^- ions (red circles) are already in the membrane in the vicinity of NH_2^+ groups (green stars), while none of cations have even penetrated the membrane. This is likely a consequence of the attractive interaction between Cl^- ions and the NH_2^+ groups, which lessens the energy barrier for Cl^- to penetrate the membrane compared to cations.[39]

At 10 ns, Cl^- ions continue to penetrate into the membrane and move further toward the center of the membrane ($z = 0$ Å). On the other hand, monovalent Li^+ (black triangles) and divalent Mg^{2+} (blue squares) display different transport behaviors. Our simulations indicate that a significant number of Li^+ ions are closely associated with Cl^- ions, predominantly within a few angstroms of adjacent Cl^- counter-ions situated at the membrane's center. However, only one Mg^{2+} ion manages to overcome the Coulombic repulsion at the membrane feed surface to reach the center of the membrane. It is likely that Cl^- ions can chaperone either cation species through the membrane, based on both Li^+ and Mg^{2+} ions being near Cl^- ions. This observation is consistent with experimental evidence of cation–anion transport coupling in our prior study.[39] However, Cl^- ions here are more likely to chaperone Li^+ because Mg^{2+} ions have stronger repulsive interactions with NH_2^+ groups near the feed surface of the membrane. This creates a large electrostatic barrier for Mg^{2+} to get transported into the membrane and makes the coupled transport even less likely.

By 50 ns, a few Cl^- ions have reached the permeate. Simultaneously, feed ions begin to accumulate in a low-density region near the center of the membrane (light gray area visible in Figure $5A_2$). This ion cluster consists mainly of Cl^- and Li^+ ions, as approximately 60% of the Mg^{2+} ions have not yet penetrated the membrane. The cluster of Li^+ and Cl^- ions is likely encountering steric hindrance, slowing further movement through the membrane.

At the end of the simulation at 100 ns, 12% of the Cl^- ions have reached the permeate. Meanwhile, 87% of the Li^+ ions have crossed the membrane's center, while two-thirds of the Mg^{2+} ions have not yet penetrated the membrane, as shown in Figure $5A_4$. This results in a net negative charge in the permeate, likely due to the limited 100 ns time scale of the simulations. We hypothesize that over longer periods, the permeate will eventually achieve charge neutrality.

Evidently, the three ion species exhibit different transport behaviors due to the ion-membrane and ion-ion interactions. The spatial distributions at 100 ns for Li^+ and Cl^- are bi-modal, as shown in Figure $5A_5$, with the Li^+ peak within the membrane slightly closer to the permeate than the Cl^- peak. Although Li^+ ions and NH_2^+ groups have repulsive interactions, the nearly overlapping peaks in the Li^+ and Cl^- distributions suggest that Cl^- facilitates Li^+ transport through the NH_2^+ groups near the feed surface, consistent with prior experimental evidence.[39] Additionally, the peak in the permeate indicates that some Cl^- and Li^+ ions reach the permeate ($z > 25$Å), as shown in Figure $5A_4$. The Mg^{2+} distribution is skewed toward the feed surface of the membrane, near the densest region of NH_2^+ groups, with other Mg^{2+} ions distributed across the membrane thickness. This suggests that

Mg^{2+} transport is most likely hindered at the membrane surface by the NH_2^+ charge, an observation consistent with the expected behavior of Donnan exclusion.

To examine how selectivity varies with concentration, we analyzed the same membrane system at pH 2 but with a feed concentration of 50 g L^{-1} TDS, as depicted in Figure 5B. Initially, at 1 ns, nearly all feed ions are situated at the membrane surface. By 10 ns, approximately 15% of the ions have migrated to the center of the membrane, and several Cl^- ions are on the verge of exiting the membrane. At 50 ns, a few Cl^- ions (4%) have permeated through the membrane, and several Li^+ ions are approaching the permeate side of the membrane surface. Additionally, most Cl^- and Li^+ ions have infiltrated the membrane, whereas a third of the Mg^{2+} ions have not yet penetrated it. By the end of the simulation at 100 ns, 10% of the Cl^- ions and less than 5% of the Li^+ and Mg^{2+} ions have traversed the membrane. However, many ions cluster near the membrane center, akin to the lower pH scenario in Figure $5A_4$, due to the loose polymer nanostructure at this location, which impedes their diffusion to the permeate side.

Figure $5B_5$ shows that the distribution of all three ion species peaks near the center of the membrane, just past the densest region of NH_2^+ functional groups (green). However, the Li^+ distribution is somewhat broader than that of Mg^{2+} and Cl^-, suggesting a stronger association between Li^+ and Cl^-. The higher feed concentration appears to facilitate the chaperoning of Mg^{2+} ions by nearby Cl^- ions, a behavior different from that observed at lower concentrations. Additionally, the increased availability of Cl^- ions to associate with NH_2^+ groups seems to allow Mg^{2+} ions to move through the membrane with reduced repulsion.

At the higher pH 7, shown in Figure 5C,D, both NH_2^+ (green stars) and COO^- (gold diamonds) functional groups are present, and the transport behavior of the ions is quite different from pH 2. At a low feed concentration of 10 g L^{-1} TDS in Figure 5C, Li^+ ions quickly associate with COO^- groups near the membrane's feed surface (1 and 10 ns in Figure $5C_2$). As the simulations progress, Cl^- ions migrate through the membrane due to attractive interactions with NH_2^+ groups, evident near the center of the membrane in Figure $5C_2$–C_4, in spite of the repulsion from the COO^- groups near the membrane surface. Consequently, it is likely that Cl^- ions hop from one NH_2^+ to another to permeate through the membrane. By 100 ns, 30% of the Cl^- ions reach the permeate. In spite of this, there are still some Cl^- ions in the feed due to the repulsion of the COO^- groups. Furthermore, both cation species, regardless of valency, remain stuck on the feed surface of the membrane, strongly associated with COO^- groups, even after 100 ns (Figure $5C_4$). This is reflected in the probability distributions at 100 ns in Figure $5C_5$, where Li^+ and Mg^{2+} are clustered at the feed surface where COO^- groups are concentrated. On the other hand, Cl^- ions are spread out across the thickness of the membrane and into the permeate reservoir.

At higher solute concentrations at pH 7 in Figure 5D, Cl^- ions still migrate faster than the cations, with some Cl^- ions associating with NH_2^+ groups after penetrating the negatively charged layer on the membrane surface, as illustrated in Figure $5D_3$–D_4. At 100 ns, fewer than 10% of the Cl^- ions permeate through the membrane, compared to 30% at pH 2. Most Cl^- ions are on the membrane surface, pairing with cations, which are simultaneously attracted to the COO^- groups. Although both cations have strong association with the the COO^- groups, some Li^+ ions
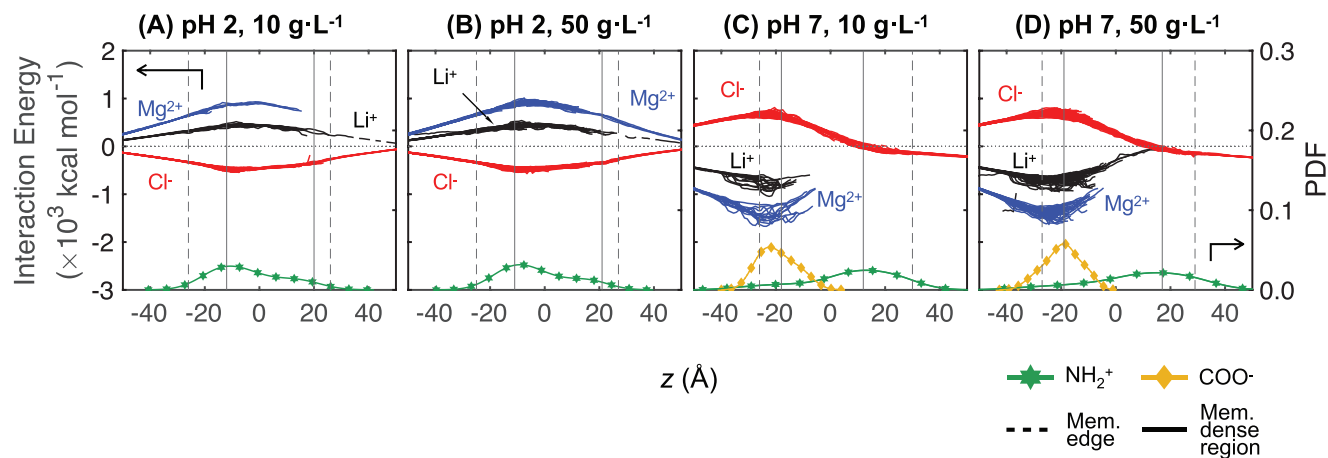
Figure 6. Interaction energy between feed ions and uncoated polyamide membranes in the z-direction of membrane thickness (left vertical axis) across all trials: A) pH 2, 10 g L^{-1}, B) pH 2, 50 g L^{-1}, C) pH 7, 10 g L^{-1}, and D) pH 10, 50 g L^{-1}. Probability density functions of NH$_2^+$ and COO$^-$ are plotted on right vertical axis. Dashed vertical lines mark the edge-to-edge boundaries of the membrane model, and solid vertical lines bound the densest regions of the membrane.

manage to penetrate past the center of the membrane by 100 ns. In contrast, none of Mg^{2+} ions move past membrane surface. The distribution of ions in Figure 5D$_5$ reinforces how cations get stuck near the membrane feed surface, overlapping the COO$^-$ distribution. The COO$^-$ layer appears to play the role of a barrier, preventing Li$^+$ and Mg^{2+} from penetrating. At the same time, the cations appear to associate with Cl$^-$ ions near the feed surface, which increases steric repulsion.

Comparing Figure 5A$_5$ and B$_5$, Li$^+$/Mg^{2+} selectivity decreases as concentration increases at pH 2. Similarly, for a feed concentration of 10 g L^{-1}, Li$^+$/Mg^{2+} selectivity decreases as the feed pH increases from 2 to 7. These trends agree with experimental findings illustrated in Figure 4B. Comparing Figure 5C$_5$ and D$_5$, selectivity is less affected by concentration at pH 7, although Li$^+$ ions permeate slightly further into the membrane than Mg^{2+} ions at the higher concentration, consistent with Figure 4B. Despite the constrained length and time scales of MD simulations, it is evident that ion-ion and ion-membrane interactions strongly influence ion partitioning, depending on concentration and pH.

In order to better understand non-steric ion-membrane interactions, we use the NAMDEnergy tool to calculate the net interaction energetics (both electrostatic and van der Waals contributions, although electrostatic contributions dominate) between each feed ion and all of the charged functional groups throughout the membrane. In **Figure 6**, the left vertical axis indicates the interaction energy of each solute ion with the membrane as a function of the solute ion location in the z-direction over the entire course of the simulations (100 ns) at an interval of 0.01 ns (one line for each ion with all ions superimposed). The energetics here only represent the interaction between each solute ion and the membrane charge in a vacuum, as if no water is present. Steric effects and water solvation, which can contribute to steric effects, are not taken into account. Since the interaction energy in an aqueous environment is complex, we utilize this methodology only to provide a simplified yet straightforward characterization of ion-membrane interaction energy at the molecular level. As a result, the relative magnitudes of energy are more significant than the absolute numerical values. To display the effect

of NH$_2^+$ and COO$^-$ functional groups on the interaction energy landscape, we also show the probability density function of membrane functional groups (right vertical axis) in Figure 6.

For membrane systems simulated at pH 2 with 10 g L^{-1} TDS feed solutions in Figure 6A, all ions in the feed reservoir at z < -40 Å have very low interaction energies with membrane charges due to the large spatial separation. As the external body force moves feed ions toward the membrane in +z-direction, the Cl$^-$ interaction energies become more negative, indicating more attractive interactions with NH$_2^+$ groups in the membrane. Their interaction energy reaches the lowest value near z = −10 Å, coinciding with the highest local density of NH$_2^+$ functional groups. As z increases further, the distance to the highest density of NH$_2^+$ groups decreases, and the Cl$^-$—NH$_2^+$ interaction energies decrease, eventually diminishing to zero in the permeate where the Cl$^-$ ions are far from the NH$_2^+$ groups in the membrane.

For Li$^+$ and Mg^{2+}, the interaction energy is positive, indicating the expected repulsive interaction between the cations and the positively charged NH$_2^+$ groups. The interaction energy for Mg^{2+} is about twice that for Li$^+$, as would be expected based on the cation charge. The Mg^{2+} interaction energy curve does not extend across the entire membrane because no Mg^{2+} ions permeate through the membrane by the end of the simulation. The stronger repulsive interaction energy with the positive NH$_2^+$ groups near the feed surface for Mg^{2+} than Li$^+$ is consistent with the results in Figure 5A$_5$, as most Mg^{2+} ions get stuck on the membrane feed surface while some Li$^+$ ions proceed to the permeate by the end of the simulation. The interaction energy profiles for pH 2 with 50 g L^{-1} TDS, shown in Figure 6B, are very similar to those at the lower concentration, because the interaction energies are independent of solute concentration. However, some Mg^{2+} energy profiles extend into the permeate, as some Mg^{2+} ions make it through the membrane to the permeate at the higher concentration. Nevertheless, in spite of similar interaction energy profiles for the two concentrations, the progress of the two cations differs substantially, as is evident in Figure 5A$_5$ and B$_5$, because of the combined impact of charge and steric effects.

**ADVANCED
SCIENCE NEWS**

www.advancedsciencenews.com

**ADVANCED
FUNCTIONAL
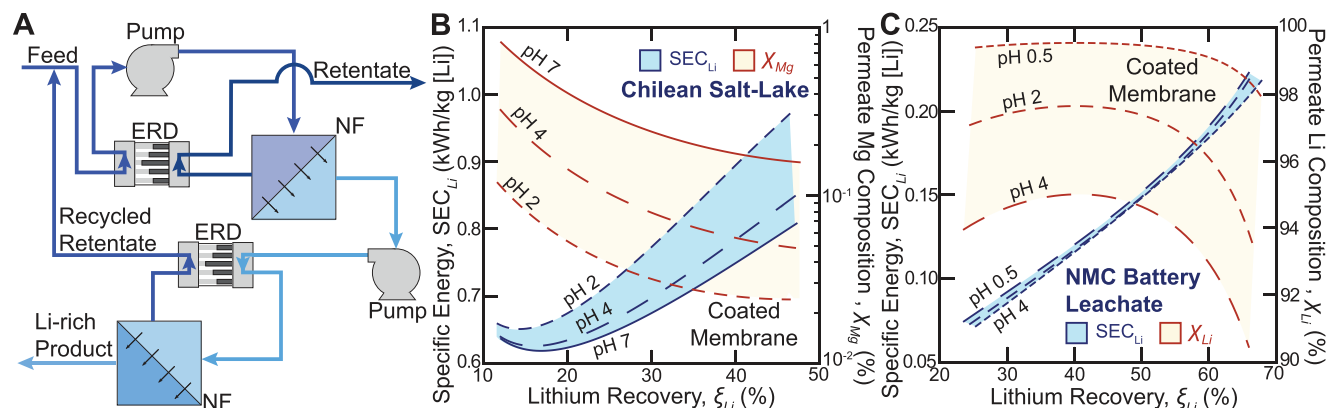MATERIALS**

www.afm-journal.de

Figure 7. A) Schematic diagram illustrating the feed, permeate and retentate streams, energy recovery device (ERD) and the high pressure pumps in a two-stage nanofiltration process. B) Plot of the projected specific energy consumption and the permeate Mg composition as a function of the solution pH and the lithium recovery from 250 g L^{-1} Chilean salt-lake brine with the polyelectrolyte-coated membrane. C) Plot of the projected specific energy consumption and the product Li purity as a function of the solution pH and the lithium recovery from NMC battery leachates with the polyelectrolyte-coated membrane.

For pH 7 systems (Figure 6C,D), the interaction energy profiles are opposite in sign from pH 2 systems due to attractive interactions between the cations, Li$^+$ or Mg^{2+}, and COO$^-$ groups near the membrane surface. On the other hand, Cl$^-$ interactions with COO$^-$ groups are repulsive. A broader range of interaction energies is evident at pH 7 than at pH 2, particularly for Li$^+$ or Mg^{2+} ions in the vicinity of the membrane surface. This comes about because of the variability of x-, y-locations of the ions with respect to the COO$^-$ groups at the membrane surface. Once Li$^+$ or Mg^{2+} ions make it past the surface COO$^-$ groups, the interaction energies are less attractive, although no cations make it all the way to the permeate. Cl$^-$ ion interaction energies are positive (repulsive) near the feed surface of the membrane where COO$^-$ groups dominate. However, further into the membrane, in the vicinity of NH$_2^+$ groups, and extending into the permeate, the interaction energy becomes negative, reflecting the attraction between Cl$^-$ ions and NH$_2^+$ groups in the membrane. Had any Li$^+$ or Mg^{2+} ions reached the permeate side of the membrane, the interaction energy would be positive (repulsive) because of the proximity to the NH$_2^+$ groups. Referring back to the hindered propagation of Li$^+$ and Mg^{2+} through the membrane in Figure 5C$_5$ and D$_5$, it is evident from Figure 6C,D that the strong charge interactions are responsible.

The MD simulation results in Figures 5 and 6 reveal the role of membrane functional groups on mono-/divalent ion partitioning and also ion transport mechanisms at the molecular level. The main focus of MD simulations here is to investigate the effect of different charged functional groups in the membrane. While the membrane models used for MD simulations do not directly represent the coated membranes used for our experimental studies, the MD studies capture the primary interactions. Since the experimental membrane coating primarily consists of NH$_2^+$ groups, as noted in Section 2.1, its effect is similar to that of NH$_2^+$ groups on permeating ions is evident in the pH two conditions of the MD simulations. Thus, the MD simulations provide molecular-level insights in terms of interaction mechanisms and spatial relationships of NH$_2^+$ groups on ion selectivity.

2.4. Donnan-Enhanced Nanofiltration is Operationally Effective for Salt-Lake and Battery Leachate Lithium Concentration

Lastly, we correlate the improvements in cation selectivity, driven by nanoscale transport mechanisms as elucidated by our MD analyses, with the consequent enhancements in the performance metrics of macroscale NF spiral-wound modules. Through this analysis, we quantify the potential improvements in thermodynamic efficiency that could be realized in industrial NF treatment processes utilizing the Donnan-enhanced membranes. Here, we project the specific energy requirement of a two-stage NF process, as outlined in Section Module Performance Evaluation, which has been commercialized for desalination pretreatment and resource recovery.[77,78] As illustrated in **Figure 7A**, we analyze a two-stage NF treatment system employing the polyelectrolyte-coated membrane to concentrate lithium from Chilean salt-lakes and NMC battery leachates. Using the calibrated DSPM-DE model for ion transport, as detailed in Section 2.1 and Figure S5 to S13 (Supporting Information), we calculate nodal ion fluxes as a function of the feed salinity, composition, and acidity. The DSPM-DE model, which is subsequently integrated with a Forward Euler scheme, facilitates the projection of lithium recovery rates, permeate purity, and net electrical work consumption achievable with a spiral-wound module. Specifications for the spiral-wound element are derived from a commercially available module (Nitto-Denko PRO-XS1) that employs the same polyelectrolyte-coated NF membrane. The isentropic efficiencies of the high-pressure pump and energy recovery device are assumed to be 0.75 and 0.80, respectively.[79]

Figure 7B presents the specific energy consumption (SEC$_{Li}$) and residual Mg concentration (χ_{Mg}) in the retentate stream of a two-stage NF process, as a function of the lithium recovery rate (ξ_{Li}) and solution pH. With Chilean salt-lake brines, the specific electrical work consumption escalates with decreasing pH levels and with the addition of the surface coating, across the range of lithium recovery rates. As discussed previously, the addition of the polyelectrolyte coating reduces the permeate flux by up to 18% at a given driving pressure. Further, with the coated

**ADVANCED
SCIENCE NEWS**

www.advancedsciencenews.com

**ADVANCED
FUNCTIONAL
MATERIALS**

www.afm-journal.de

membrane, at a lithium recovery rate of 30%, the SEC_{Li} experiences a 14.7% increase from 0.673 to 0.772 kWh kg^{-1} as the solution pH decreases from 7 to 2. This increment is ascribed to the diminished permeability of lithium cations, which is a consequence of the enhanced Donnan exclusion effect with coated membranes in acidic conditions.[33,48] This observation is consistent with the coupon-scale experiments and is proportionally reflected in the specific electrical work required per mole of lithium recovered, as depicted in Figure 7B. Furthermore, the SEC of the two-stage NF process increases with lithium recovery rates across the tested pH levels, attributable to the increased least work of separation necessitated by higher pressures for permeate production — a finding in alignment with the augmented osmotic pressures observed during high recovery separations in pressure-driven membrane processes.[80]

Conversely, the two-stage NF process benefits from enhanced Donnan exclusion effects, which disproportionately increase the rejection of Mg^{2+} ions relative to Li$^+$ ions, resulting in permeate streams with lower concentrations of multivalent cations across the range of lithium recovery rates tested. Figure 7B and Figure S14A (Supporting Information) depict the residual Mg^{2+} composition as a function of the lithium recovery rate and solution pH, comparing uncoated and coated membranes. Our analysis reveals that two-stage NF systems utilizing the coated membranes yield permeate streams richer in monovalent ions, with the residual permeate Mg^{2+} concentration decreasing by 25% at pH 7, and by 39% at pH 2, following the application of the polyelectrolyte coating. With coated membranes, a significant further reduction in Mg^{2+} concentration in the permeate from 0.23% to 0.031% is observed as the solution pH decreases from 7 to 2, exemplifying how Donnan exclusion enhances the efficacy of cation separation in spiral-wound applications.

Our analysis underscores the practical implications of the permeability-selectivity trade-off in system scale NF separations. Donnan-enhanced NF processes show higher specific energy consumption due to reduced ion fluxes and reduced recovery rates under constant driving pressure, but concurrently show enhanced permeate quality due to significantly reduced concentration of the undesired ion species (e.g., Mg^{2+}). In two-stage NF systems employing the coated membrane, an order-of-magnitude reduction in undesired Mg^{2+} ion permeate concentration is accompanied by an increase of SEC_{Li} of merely 14.7%, which confers net operational benefits for salt-lake lithium concentration.

Figure 7C illustrates the specific energy consumption and permeate lithium purity of a two-stage NF process employing the coated membranes for lithium extraction from NMC leachates, as a function of the solution pH and lithium recovery rate. Likewise, a similar module-scale analysis conducted with NMC battery leachates reveals that specific energy consumption increases with lithium recovery rates, consistent with the Second Law of Thermodynamics.[81] Notably, our results suggest that the attainable lithium recovery rates from battery leachates are higher as compared to Chilean salt lakes, which may be attributed to the lower total dissolved solid concentration and osmotic pressure of the leachate.[81]

Our computational findings, which are summarized in Figure 7C and Figure S14B (Supporting Information), underscore the efficacy of the two-stage NF system in extracting lithium from mixed metal battery leachates, achieving lithium purity levels great than 99.5% in the permeate stream. Analogous to the analysis conducted for salt-lake brines, the observed selectivity enhancement is attributed to the augmented Donnan exclusion effect, which facilitates lithium ion passage while effectively obstructing the transport of multivalent ions such as Co^{2+}, Mn^{2+} and Ni^{2+}. For instance, the introduction of the positively-charged polyelectrolyte coating enhances the resultant lithium purity of the permeate by 0.6% and 2.0% at pH 4 and 0.5, respectively. With coated membranes, a further increase in Li$^+$ permeate composition from 95.0% to 99.5% is registered with greater NH$_2^+$ functional group density, when the solution pH decreases from 7 to 2. Cumulatively, in two-stage NF systems employing the coated membrane, a near order-of-magnitude reduction in Co^{2+}, Mn^{2+} and Ni^{2+} permeation is accompanied by a modest increase in SEC_{Li} by approximately 5%. In essence, the use of coated membranes leads to notable improvements in the lithium composition of the permeate, underscoring the operational advantages conferred by improvements in monovalent selectivity for the recovery of lithium from expended battery leachates.

3. Conclusion

In this work, we develop and characterize nanofiltration (NF) membranes specifically engineered for monovalent selectivity from high salinity brines, facilitating lithium concentration from salt-lakes and battery leachates. We introduce a highly permeable polyelectrolyte surface coating, endowed with a high density of positively charged ammonium functional groups, onto conventional polyamide membranes. This modification significantly bolsters the membrane's selectivity for monovalent ions, while sustaining high cation permeability. Consequently, the coated NF membrane exhibits enhanced Donnan exclusion, which decreases multivalent cation permeation (e.g., Mg^{2+}, Mn^{2+}, Co^{2+}, and Ni^{2+}) by an order-of-magnitude while reducing monovalent cation permeation by only about 25%.

By characterizing the electrokinetic slip planes and the functional groups present in the active layer, we show that the coated membranes maintain a consistent positive surface charge over the pH range of 1 to 8, which is attributed to the high density of positively charged ammonium functional groups within the surface coating. Additionally, leveraging an original experimental dataset that comprises over 8000 ion rejection measurements obtained using our bench-scale setup, we demonstrate that the coated membrane is capable of refining salt-lake brines to a residual magnesium concentration of 0.14%, and upgrading battery leachates to a lithium purity of 98% through a singular stage NF process. Moreover, our experiments reveal that the ion rejection efficacy of the membrane is preserved, even after prolonged exposure to acidic feeds for up to 12 weeks. Compared to membranes documented in existing literature, our coated NF membrane emerges as a non-dominated solution, striking a balance between selectivity and permeability for dual-objective optimization.

Further, we employ molecular dynamics (MD) simulations to gain mechanistic insights into the interactions between feed ions and the charged functional groups within the membrane. Our analysis of polyamide NF membranes elucidated a Coulombic attraction formed between carboxylate functional groups and

cations and an energy barrier in interactions between ammonium functional groups and cations. The latter aids in impeding the transport of multivalent cations. The MD simulations indicate that the improvement in selectivity for monovalent ions stems from the slower kinetics of ion partitioning, attributed to the greater electrostatic barrier encountered by multivalent cations in polyamide membranes enriched with higher densities of ammonium groups. These molecular-level findings are in agreement with our membrane characterization results, suggesting that charge-based screening effects are pivotal in enhancing monovalent selectivity.

By employing module-scale analysis, we quantify potential enhancements in thermodynamic efficiency achievable in industrial NF treatment processes using Donnan-enhanced coated membranes. Specifically, we focus on a two-stage NF process aimed at concentrating lithium from Chilean salt-lakes and NMC battery leachates, employing the calibrated DSPM-DE model for ion transport to project specific energy requirements and permeate quality. Our analysis revealed that the addition of the polyelectrolyte coating increases specific energy consumption (SEC_{Li}) by up to 14.7% when concentrating lithium from Chilean salt-lake brines. Despite this increase, the benefits of the coating are pronounced in the enhanced rejection of Mg^{2+} ions relative to Li^+ ions, resulting in permeate streams with significantly lower concentrations of multivalent cations. Specifically, the residual Mg^{2+} concentration was reduced by up to 39% at pH 2, producing permeate streams with a residual Mg^{2+} composition of 0.031%. For NMC battery leachates, our findings suggest that the coated membranes can achieve lithium purity levels exceeding 99.5% in the permeate stream, with a modest increase in SEC_{Li} of approximately 5%. This illustrates the operational advantages of using coated membranes for the recovery of lithium from salt-lakes and battery leachates, highlighting the balance between a minor increase in energy consumption and significant improvements in permeate quality.

In conclusion, while our tailored nanofiltration membranes substantially mitigate multivalent cation concentrations and elevate the purity of lithium in both hypersaline brines and battery leachates, the challenge of distinguishing between monovalent ions such as Li^+ and Na^+ remains. Given the high concentration and similar ionic characteristics of sodium compared to lithium, the reliance on Donnan exclusion alone has proven inadequate to impart selectivity between these monovalent ions. However, even partial improvements in Li^+/Na^+ selectivity could significantly reduce the usage of chelants and absorbents in downstream Direct Lithium Extraction (DLE) processes. Future investigations will thus focus on refining membrane technologies to include specific enhancements, such as advanced surface coatings or novel structural adaptations, aimed explicitly at improving Li^+/Na^+ separation.

4. Experimental Section

Chemicals and Materials: Two types of semi-aromatic nanofiltration (NF) membranes were fabricated by Nitto-Denko (Shiga, Japan). First, the pristine membrane features a polyamide active layer polymerized on a polysulfone support that was woven into a polyester mesh; the polyamide active layer was the product of the canonical interfacial polymerization reaction between piperazine and trimesoyl chloride.[32] Second, a highly

cross-linked and acid-tolerant polyelectrolyte was covalently condensed with the carboxyl functional groups in the polyamide layer, yielding a positively-coated Donnan-enhanced composite NF membrane.[50] The NF membranes were stored in a 10 g L^{-1} NaCl solution and soaked in deionized water for 24 h before use. The feed and permeate channel spacers were procured from a commercial spiral wound membrane module.

Bench-scale experiments were conducted using salt-lake brines and battery leachates to characterize the selectivity of the coated and uncoated membranes. Anhydrous chlorides and sulfates of Na^+, K^+, Li^+, Mg^{2+}, Mn^{2+}, Co^{2+}, and Ni^{2+}, as well as NaOH (> 98%) and HCl (37%), were procured from MilliporeSigma. Polyethylene glycols with molecular weights of 62, 200, 400 and 600 g mol^{-1} were procured from Fisher Scientific. Type I ultrapure water (18.2 MΩ cm) was used to prepare all stock solutions. The synthetic salt-lake brines were based on the actual aqueous compositions of Salar de Atacama, Chile and Qaidam Lake, China[39] (**Table 1**). The synthetic battery leachates correspond to the products from the inorganic acid leaching of $LiNi_xMn_yCo_{1-x-y}O_2$ (NMC)[18] and Li_2MnO_2 (LMO)[17] battery cathodes (**Table 2**). The rationale for the choice of feed solution was delineated in the Supporting Information.

Membrane Characterization: The surface morphology of the uncoated and coated membranes were examined with field emission scanning electron microscopy (FE-SEM, Hitachi S-4800) at an acceleration voltage of 5 kV. To study the polyelectrolyte and polyamide active layers within the membrane's cross-section, transmission electron microscopy (TEM, Philips CM 100) was employed. The zeta potential and charge density of the membranes' diffuse layer were assessed with streaming potential experiments (Anton SurPASS 3 Electrokinetic Analyzer). Fourier transform infrared spectroscopy (FTIR, Nicolet iS50 FTIR Spectrometer) was utilized to identify the charged functional groups present in the active layer. The hydrophilicity of the active layer was determined with water contact angle measurements (Ossila Contact Angle Goniometer). The ion partitioning of the membranes was examined with quartz crystal microbalance with dissipation experiments (QCM-D, E4, QSense Biolin Scientific).

In this study, a bench-scale plate-and-frame module was utilized to evaluate the permeability and selectivity of both coated and uncoated NF membranes.[39] Detailed information on the experimental configuration can be found in the Supporting Information (please see Section S2.1, Supporting Information). Within the module, a coupon measuring 8.0 cm by 3.0 cm was accommodated, and it features feed and permeate channels that were separated by spacers, each 1 mm in thickness. The flow loop was equipped with pulsation dampeners (Hydra-Cell 4CI SST) and a temperature control system to regulate the pressure and temperature of the feed solution. The permeate flux was determined based on gravimetry (Ohaus Scout Pro SP601), and the solution conductivity and pH levels (Hach HQ440d) were monitored and recorded at 1 Hz frequency on LabView. To assess the aging performance in acidic leachates, pristine NF membranes were submerged in a 0.5 M HCl solution for up to 12 weeks, and ion rejection experiments with salt-lake brines and battery leachates were periodically conducted.

Cumulatively, over 8000 ion rejection measurements, corresponding to 1152 unique permeate samples, were collected using the bench-scale apparatus. Each sample represented a distinct operating condition, encompassing solution pH values ranging from 0 to 7 and feed salinities from 10 g L^{-1} to 250 g L^{-1}, across two distinct salt-lake brines and two compositions of battery leachates. The experimental data was comprehensively compiled in the Supporting Information (Section S2.2, Supporting Information). The bench-scale experiments were conducted at a cross-flow velocity of 0.17 m s^{-1}, and at a temperature of 20 ± 0.5 °C. The membrane coupon was first installed and compacted under high pressure of 50 bar for 2 h. Thereafter, the membrane was contacted with the saline feed solution for at least 15 min at the specific pressure before the feed and permeate solutions were sampled. The sampled solutions were collected in centrifuge tubes and chilled. Thereafter, the ionic compositions were measured with inductively coupled plasma optical emission spectroscopy (Agilent ICP-OES 5100), using five-point standards from MilliporeSigma (Trace-Cert). Based on triplicate sampling, the maximum uncertainty in the concentration measurements were below 4.3%. For molecular weight cutoff characterizations, a total organic carbon analyzer was employed (Elementar

**ADVANCED
SCIENCE NEWS**

www.advancedsciencenews.com

**ADVANCED
FUNCTIONAL
MATERIALS**

www.afm-journal.de

Table 1. Ionic composition of the salt-lake brine from Salar de Atacama, Chile and Qaidam Lake, China.[39]

Salt Lake, Location	Nominal Composition (g L^{-1})						
	Li$^+$	Na$^+$	K$^+$	Mg^{2+}	Cl$^-$	SO$_4^{2-}$	TDS
Salar de Atacama, Chile	1.19	69.01	17.89	7.31	143.72	12.06	251.18
Qaidam Lake, China	0.31	56.30	4.40	20.20	134.20	34.10	249.51

Vario-EL Cube). The pore size distribution of the coated and uncoated membranes was estimated using polyethylene glycol (PEG) rejection tests with molecular weights of 62, 200, 400, and 600 g mol^{-1}, at pH levels of 7, 4, and 2. The organic solute rejection was correlated using nonlinear least squares regression and a Monte Carlo approach to calculate the molecular weight cut-off (MWCO) and average pore radius, accounting for measurement uncertainties.[35,49,82] The zeta potential is calculated from the streaming potential measurements with the classical Smoluchowski equation. The QCM-D experiments were conducted based on the method proposed by Villalobos et al.,[66] and the fundamental resonance frequency changes were recorded with 0.1 M LiCl and MgCl$_2$ solutions at pH 2 and 7, to elucidate the impacts on solute partitioning.

The transmembrane water flux was calculated based on gravimetry, as determined by Equation (1). The water permeabiltiy coefficient can be calculated with Equation (2), based on experiments with ultrapure water

$$J_w = \frac{\Delta m}{\rho_w A_m \Delta t} \tag{1}$$

$$A_w = \frac{J_w}{\Delta P} \tag{2}$$

where J_w [L m^{-2} h^{-1}] and A_w [L m^{-2} h^{-1} bar^{-1}] represent the transmembrane water flux and water permeability coefficient, ρ_w [kg L^{-1}] and A_m [m^2] denote the solution density and membrane cross-sectional area, Δm [kg], Δt [s] and ΔP [bar] denote the change in permeate mass, process time and transmembrane pressure, respectively. The species rejection was calculated based on Equation (3), using concentrations as determined by ICP-OES. The separation factor between species i and j was determined based on Equation (4).

$$R_i = 1 - \frac{C_{i,p}}{C_{i,f}} \tag{3}$$

$$\alpha_{i,j} = \frac{C_{i,p}/C_{j,p}}{C_{i,f}/C_{j,f}} \tag{4}$$

where R_i [-] and $\alpha_{i,j}$ [-] denote the species rejection and separation factor, $C_{i,p}$ [mol L^{-1}] and $C_{i,f}$ [mol L^{-1}] represent the concentration of species i in the permeate and feed solutions, respectively.

Molecular Dynamics Analysis: To complement the experimental investigation, molecular dynamics simulations were employed to elucidate interaction dynamics between feed ions and charged functional groups within the membrane. The polyamide active layer was simulated, not the porous support structure that was typical of commercial thin-film composite NF membranes. The membrane models were virtually polymerized us-

ing piperazine and trimesoyl chloride monomers,[83,84] typical of NF membranes such as NF270. The number density and distribution of NH$_2^+$ and COO$^-$ functional groups within the membrane models were based experimental measurements at different feed pH conditions,[38] as shown in Figure S1B,C (see Supporting Information) for feed pH 2 and 7, respectively.

Before production simulations of solute transport, virtually polymerized membrane models need to be equilibrated using counter-ions to neutralize the charged functional groups within the nanostructures of the polyamide active layer (see Figure S2, Supporting Information).[84] After equilibration of the charged membrane nanostructure, the membrane model was placed between identical feed and permeate reservoirs (50 × 50 × 45 Å^3, after further equilibration), as depicted in Figure S3C (Supporting Information), corresponding to the membrane's dimensions in the *x*- and *y*-directions and using periodic boundary conditions. Single-layer graphene sheets bounding each reservoir bear an externally applied pressure of 0.1 MPa, thus maintaining a net zero transmembrane pressure. In the feed reservoir, the dilute solution had 5 Li$^+$, 5 Mg^{2+}, and 15 Cl$^-$ ions, corresponding to 10 g L^{-1} TDS (precisely, 10.04 g L^{-1}) of LiCl and MgCl$_2$; the concentrated solution has 25 Li$^+$, 25 Mg^{2+}, and 75 Cl$^-$ ions, corresponding to roughly 50 g L^{-1} TDS (precisely, 50.20 g L^{-1}) of LiCl and MgCl$_2$. The permeate reservoir contains only water molecules.

To facilitate the transport of solute ions across the membrane in the short time that was practical to simulate, a body force was applied in the positive *z*-direction to each feed ion.[85–87] The magnitude of this force was proportional to the ion's Coulombic charge, effectively simulating an external electric field of 0.5 V.[88] Specifically, a force of 0.072 kcal mol^{-1}Å^{-1} was exerted on monovalent ions (Li$^+$ and Cl$^-$) and 0.144 kcal mol^{-1}Å^{-1} on divalent ions (Mg^{2+}).[88] This approach ensured accelerated ion movement through the membrane without causing ion clustering at the membrane surface or disrupting the membrane structure. Each simulation started with all ions in the feed reservoir and extends for 100 ns. Three independent runs were performed to ensure repeatability. Since the primary focus of these simulations was on solute-membrane charge interactions, there was no transmembrane pressure and reservoir sizes remain constant throughout the simulation. All MD simulations were conducted with the Nanoscale Molecular Dynamic (NAMD) simulation package,[76] in conjunction with the General AMBER Force Field (GAFF).[89–91]

Module Performance Evaluation: The Donnan-steric pore model with dielectric exclusion (DSPM-DE) was calibrated with the ion rejection measurements to facilitate module-scale analysis of a two-stage NF process employing the positively-coated membranes.[35] A full account of the model, encompassing numerical assumptions, limitations, and the solution algorithm, is provided in the Supporting Information (see Section S1.2, Supporting Information). In the DSPM-DE model, species

Table 2. Ionic composition of the acid leachate from NMC and LMO battery cathodes.[17,18]

Battery Cathode Leachate	Nominal Composition (g L^{-1})						
	Li$^+$	Mn^{2+}	Co^{2+}	Ni^{2+}	H$_3$O$^+$	Cl$^-$	TDS
LiNi$_x$Mn$_y$Co$_{1-x-y}$O$_2$ (NMC)	2.31	3.31	14.16	4.27	5.71	48.91	78.67
Li$_2$MnO$_2$ (LMO)	1.17	1.15	0.06	0.01	5.71	18.18	26.28

2408685 (14 of 17)

**ADVANCED
SCIENCE NEWS**

www.advancedsciencenews.com

**ADVANCED
FUNCTIONAL
MATERIALS**

www.afm-journal.de

transport was described by the extended Nernst-Planck partial differential equation, incorporating concentration-driven diffusion, electrostatically-driven electromigration, and bulk transport by advection, as described by Equation (5)[28]

$$N_i = K_{i,a} c_i J_w - K_{i,d} D_{i,\infty} \nabla c_i - K_{i,d} D_{i,\infty} \frac{z_i c_i F}{RT} \nabla \Psi \tag{5}$$

where N_i [mol m^{-2} h^{-1}] represents the net solute molar flux, $K_{i,a}$ [-] and $K_{i,d}$ [-] represent the hindrance coefficients from convection and diffusion, c_i [mol L^{-1}] and z_i [-] represent the molar concentration and electronic valency, $D_{i,\infty}$ [m^2 s^{-1}] represents the diffusion coefficient, F [C mol^{-1}] and R [J mol^{-1} K^{-1}] represent the Faraday and ideal gas constants, and T [K] and Ψ [V] represent the temperature and electric potential, respectively. The boundary conditions to the partial differential equation were imposed by isoactivity conditions along the solution-membrane boundaries, as described by Equation (6).[92,93] To ensure chemical stability, electroneutrality constraints were imposed in the bulk solution and within the nanopores of the NF membrane, yielding Equations (7) and (8)[39,94]

$$\frac{(\gamma_i c_i)_{mem}}{(\gamma_i c_i)_{bulk}} = \Phi_{i,st} \, \Phi_{i,do} \, \Phi_{i,di} \tag{6}$$

$$\sum_i^N z_i c_{i,bulk} = 0 \tag{7}$$

$$\chi_d + \sum_i^N z_i c_{i,mem} = 0 \tag{8}$$

where χ_d [mol L^{-1}] represents the charge density of the active layer, $\Phi_{i,st}$ [-], $\Phi_{i,do}$ [-] and $\Phi_{i,di}$ [-] represent the partition coefficients for steric, Donnan and dielectric exclusions, $c_{i,bulk}$ [mol L^{-1}] and $c_{i,mem}$ [mol L^{-1}] represent the concentration of species i in the bulk solution and within the nanopores, respectively. In the DSPM-DE model, the four hyperparameters for each membrane were regressed independently from different subsets of experimental data, where each subset corresponds to a specific feed composition and pH level. The global optimization algorithm used for parametric estimation is detailed in the prior publication.[39]

The calibrated DSPM-DE was leveraged to project the thermodynamic performance of an industrial two-stage NF process that was commonly used for lithium concentration.[34] The DSPM-DE model was integrated using a forward Euler scheme with 100 steps to derive the final permeate stream concentrations from a spiral-wound module, using a similar numerical scheme as described in the prior publication.[39] The dimensions of the spiral-wound NF module were based on a commercially available variant (Nitto-Denko PRO-XS1) of the positively-coated NF membrane employed in this study. This spiral-wound module had a length of 1.02 m and provided an effective active area of 37.2 m^2. The permeate composition was determined by calculating the molar ratio of the cation i to the total cation concentration, as described by Equation (9).

$$\chi_i = \frac{C_{i,p}}{\sum_j^{N_{cat}} C_{j,p}} \tag{9}$$

where χ_i [-] represents the permeate composition of cation i, N_{cat} [-] denotes the number of dissolved cations, and $j \in \{$Li$^+$, Na$^+$, K$^+$, Mg^{2+}, Co^{2+}, Mn^{2+}, Ni$^{2+}\}$. The projected lithium recovery attainable by a two-stage NF system was computed based on the molar flow rate of the input feed and the lithium-rich permeate streams, as described by Equation (10)

$$\xi_{Li} = \frac{C_{Li,p} \dot{V}_p}{C_{Li,f} \dot{V}_f} \tag{10}$$

where ξ_{Li} [-] denotes the proportion of lithium recovered relative to the feed stream and, $\dot{V}_f$ [m^3 s^{-1}] and $\dot{V}_p$ [m^3 s^{-1}] represent the volumetric flow rate of the feed and permeate streams, respectively. The specific electrical energy consumption was determined relative to the molar quantity of lithium extracted following the second NF stage, as defined in Equation (11).[34] This calculation included the electrical work consumed for pumping and the flow energy reclaimed with pressure exchangers, as detailed in Equation (12)[95]

$$SEC_{Li} = \frac{\dot{W}_{in}}{C_{Li,p} \dot{V}_p \, \rho_p} \tag{11}$$

$$\dot{W}_{in} = \sum_{i=1}^{2} \left[\frac{\dot{V}_{f,i} \Delta P_{i,mem}}{\eta_{pump}} - \left(\dot{V}_{f,i} - \dot{V}_{p,i} \right) \Delta P_{i,mem} \eta_{px} \right] \tag{12}$$

where SEC_E [kWh kg^{-1}] denotes the specific energy consumption, $\dot{W}_{in}$ [W] represents the net electrical power consumed, $\Delta P_{i,mem}$ [Pa] denotes the transmembrane pressure between the feed and permeate streams in stage i, and η_{pump} [-] and η_{px} [-] represent the pump and pressure exchanger efficiencies, respectively.

Supporting Information

Supporting Information is available from the Wiley Online Library or from the author.

Conflict of Interst

Y. Tomi and T. Miyabe are affiliated with Nitto-Denko Corporation. The remaining authors declare no conflict of interest.

Author Contributions

Z.H.F. led the experiments and the module-scale analysis. S.L. led the molecular dynamics analysis. L.K. and T.L. assisted with the coupon-scale experiments. S.M.H. assisted with the partitioning measurements. Y.T. and T.M. fabricated the polyamide and polyelectrolyte membranes. S.K., R.M.L., and J.H.L. led the formal analysis and supervised the project. The manuscript was prepared and reviewed by all of the authors.

Data Availability Statement

The data that support the findings of this study are available in the supplementary material of this article.

ADVANCED
SCIENCE NEWS

www.advancedsciencenews.com

ADVANCED
FUNCTIONAL
MATERIALS

www.afm-journal.de

Keywords

battery leachate, lithium recovery, molecular dynamics, nanofiltration, salt lake

[1] T. Levin, J. Bistline, R. Sioshansi, W. J. Cole, J. Kwon, S. P. Burger, G. W. Crabtree, J. D. Jenkins, R. O'Neil, M. Korpås, S. Wogrin, B. F. Hobbs, R. Rosner, V. Srinivasan, A. Botterud, *Nat. Energy* **2023**, *8*, 1199.

[2] H. Yu, H. Yang, K. Chen, L. Yang, M. Huang, Z. Wang, H. Lv, C. Xu, L. Chen, X. Luo, *Energy Storage Mater.* **2024**, *67*, 103288.

[3] J. J. Roy, S. Rarotra, V. Krikstolaityte, K. W. Zhuoran, Y. D.-I. Cindy, X. Y. Tan, M. Carboni, D. Meyer, Q. Yan, M. Srinivasan, *Adv. Mater.* **2022**, *34*, 2103346.

[4] M. L. Vera, W. R. Torres, C. I. Galli, A. Chagnes, V. Flexer, *Nat. Rev. Earth Environ.* **2023**, *4*, 149.

[5] M. A. Alkhadra, X. Su, M. E. Suss, H. Tian, E. N. Guyes, A. N. Shocron, K. M. Conforti, J. P. De Souza, N. Kim, M. Tedesco, K. Khoiruddin, I. G. Wenten, J. G. Santiago, T. A. Hatton, M. Z. Bazant, *Chem. Rev.* **2021**, *122*, 13547.

[6] V. Flexer, C. F. Baspineiro, C. I. Galli, *Sci. Total Environ.* **2018**, *639*, 1188.

[7] K. K. Jena, A. Alfantazi, A. T. Mayyas, *Energy Fuels* **2021**, *35*, 18257.

[8] Y. Zeng, W. Li, Z. Wan, Q. Qin, Q. Huang, W. Cai, Q. Wang, M. Yao, Y. Zhang, *Adv. Funct. Mater.* **2024**, 2400416.

[9] J. Wang, X. Yue, P. Wang, T. Yu, X. Du, X. Hao, A. Abudula, G. Guan, *Renewable Sustainable Energy Rev.* **2022**, *154*, 111813.

[10] J. R. Klaehn, M. Shi, L. A. Diaz, D. E. Molina, S. M. Reich, O. Palasyuk, R. Repukaiti, T. E. Lister, *Hydrometallurgy* **2023**, *217*, 106041.

[11] T.-Y. Huang, R. Pérez-Cardona, F. Zhao, J. W. Sutherland, M. Parans Paranthaman, *ACS Sustainable Chem. Eng.* **2021**, *9*, 6551.

[12] W. Liu, D. B. Agusdinata, *J. Cleaner Prod.* **2020**, *260*, 120838.

[13] B. K. Pramanik, L. D. Nghiem, F. I. Hai, *Water Res.* **2020**, *168*, 115149.

[14] W. Lv, Z. Wang, H. Cao, Y. Sun, Y. Zhang, Z. Sun, *ACS Sustainable Chem. Eng.* **2018**, *6*, 1504.

[15] N. P. Wamble, E. A. Eugene, W. A. Phillip, A. W. Dowling, *ACS Sustainable Chem. Eng.* **2022**, *10*, 12207.

[16] S. Yasa, O. Aydin, M. Al-Bujasim, B. Birol, M. Gencten, *J. Energy Storage* **2023**, *73*, 109073.

[17] M. Shi, L. A. Diaz, J. R. Klaehn, A. D. Wilson, T. E. Lister, *ACS Sustainable Chem. Eng.* **2022**, *10*, 11773.

[18] L. A. Diaz, M. L. Strauss, B. Adhikari, J. R. Klaehn, J. S. Mcnally, T. E. Lister, *Resour., Conserv. Recycl.* **2020**, *161*, 104900.

[19] J. Li, H. Peng, K. Liu, Q. Zhao, *Adv. Mater.* **2023**, *36*, 2309406.

[20] J. Hou, H. Zhang, *Adv. Mater. Technol.* **2023**, *8*, 2201433.

[21] Z. H. Foo, C. Stetson, E. Dach, A. Deshmukh, H. Lee, A. K. Menon, R. Prasher, N. Y. Yip, J. H. Lienhard, A. D. Wilson, *Trends Chem.* **2022**, *4*, 1078.

[22] Z. Yuan, H. Liu, W. F. Yong, Q. She, J. Esteban, *Green Chem.* **2022**, *24*, 1895.

[23] K. Larsson, K. Binnemans, *Green Chem.* **2014**, *16*, 4603.

[24] Z. H. Foo, A. Deshmukh, A. D. Wilson, J. H. Lienhard, *Chem. Eng. J.* **2024**, *489*, 151159.

[25] G. Ma, Y. Xu, A. Cai, H. Mao, X. Zhang, D.-M. Shin, L. Wang, H. Zhou, *Small* **2023**, *20*, 2306530.

[26] P. Sarkar, S. Modak, S. Karan, P. Sarkar, S. Modak, S. Karan, *Adv. Funct. Mater.* **2021**, *31*, 2007054.

[27] H. Zheng, Z. Mou, Y. J. Lim, N. Srikanth, W. Zhang, S. Guo, R. Wang, K. Zhou, *Small Sci.* **2022**, *2*, 2200026.

[28] Z. H. Foo, J. B. Thomas, S. M. Heath, J. A. Garcia, J. H. Lienhard, *Environ. Sci. Technol.* **2023**, *57*, 14747.

[29] J. Ying, Y. Lin, Y. Zhang, J. Yu, *ACS ES&T Water* **2023**, *3*, 1720.

[30] Y.-L. Ji, B.-X. Gu, H.-Q. Huo, S.-J. Xie, H. Peng, W.-H. Zhang, M.-J. Yin, B. Xiong, H. Lu, L. F. Villalobos, Q. Zhao, C.-J. Gao, M. Elimelech, Q.-F. An, *Nat. Water* **2024**, *2*, 183.

[31] H. Peng, Y. Su, X. Liu, J. Li, Q. Zhao, *Adv. Funct. Mater.* **2023**, *33*, 2305815.

[32] S. Guo, Y. Wan, X. Chen, J. Luo, *Chem. Eng. J.* **2021**, *409*, 1385.

[33] H. Peng, K. Yu, X. Liu, J. Li, X. Hu, Q. Zhao, *Nat. Commun.* **2023**, *14*, 5483.

[34] R. Wang, R. Alghanayem, S. Lin, *Environ. Sci. Technol.* **2023**, *57*, 14464.

[35] R. Wang, S. Lin, *J. Membr. Sci.* **2021**, *620*, 118855.

[36] H. Zhang, Q. He, J. Luo, Y. Wan, S. B. Darling, *ACS Appl. Mater. Interf.* **2020**, *12*, 39948.

[37] P. Aydogan Gokturk, R. Sujanani, J. Qian, Y. Wang, L. E. Katz, B. D. Freeman, E. J. Crumlin, *Nat. Commun.* **2022**, *13*, 5880.

[38] C. L. Ritt, J. R. Werber, M. Wang, Z. Yang, Y. Zhao, H. J. Kulik, M. Elimelech, *Proc. Natl. Acad. Sci. USA* **2020**, *117*, 30191.

[39] Z. H. Foo, D. Rehman, A. T. Bouma, S. Monsalvo, J. H. Lienhard, *Environ. Sci. Technol.* **2023**, *57*, 6320.

[40] C. Lu, C. Hu, C. L. Ritt, X. Hua, J. Sun, H. Xia, Y. Liu, D. W. Li, B. Ma, M. Elimelech, J. Qu, *J. Am. Chem. Soc.* **2021**, *143*, 14242.

[41] X. Zhou, Z. Wang, R. Epsztein, C. Zhan, W. Li, J. D. Fortner, T. A. Pham, J. H. Kim, M. Elimelech, *Sci. Adv.* **2020**, *6*, eabd9045.

[42] C. L. Ritt, M. Liu, T. A. Pham, R. Epsztein, H. J. Kulik, M. Elimelech, *Sci. Adv.* **2022**, *8*, 5771.

[43] Y. Zhao, T. Tong, X. Wang, S. Lin, E. M. Reid, Y. Chen, *Adv. Environ. Sci. Technol.* **2021**, *55*, 1359.

[44] F. Léniz-Pizarro, C. Liu, A. Colburn, I. C. Escobar, D. Bhattacharyya, *J. Membr. Sci.* **2021**, *620*, 118973.

[45] C. Cheng, A. Yaroshchuk, M. L. Bruening, *Langmuir* **2013**, *29*, 1885.

[46] L. Ouyang, R. Malaisamy, M. L. Bruening, *J. Membr. Sci.* **2008**, *310*, 76.

[47] H. Peng, X. Liu, Y. Su, J. Li, Q. Zhao, *Angew. Chem.* **2023**, *62*, 202312795.

[48] C. Guo, C. Qian, P. Liu, Q. Zhang, X. Zeng, Z. Xu, S. Zhang, N. Li, X. Qian, F. Yu, *ACS Appl. Mater. Interfaces* **2023**, *15*, 4814.

[49] Q. Wang, Y. Wang, Y. Huang, H. Wang, Y. Gao, M. Zhao, L. Tu, L. Xue, C. Gao, *Desalination* **2023**, *565*, 116814.

[50] H. Li, Y. Wang, T. Li, X.-k. Ren, J. Wang, Z. Wang, S. Zhao, *Chem. Eng. J.* **2022**, *438*, 135658.

[51] F. A. Pacheco, I. Pinnau, M. Reinhard, J. O. Leckie, *J. Membr. Sci.* **2010**, *358*, 51.

[52] Q. Gan, C. Wu, L. Long, L. E. Peng, Z. Yang, H. Guo, C. Y. Tang, *Environ. Sci. Technol.* **2023**, *57*, 2548.

[53] H. Jaramillo, C. Boo, S. M. Hashmi, M. Elimelech, *J. Membr. Sci.* **2021**, *618*, 118568.

[54] M. Ahmad, M. Ahmed, S. Hussain, A. Ali, M. Zahra, M. I. Din, Z. Mustafa, *Desalination* **2023**, *545*, 116159.

[55] C. Y. Tang, Y.-N. Kwon, J. O. Leckie, *J. Membr. Sci.* **2007**, *287*, 146.

[56] E. Wang, S. Liu, L. Liu, L. Han, B. Su, *J. Membr. Sci. Letters* **2023**, *3*, 2772.

[57] H. Xie, T. Saito, M. A. Hickner, *Langmuir* **2011**, *27*, 4721.

[58] M. Xiao, F. Yang, S. Im, D. S. Dlamini, D. Jassby, S. Mahendra, R. Honda, E. M. Hoek, *J. Membr. Sci. Lett.* **2022**, *2*, 100022.

[59] Q. She, R. Wang, A. G. Fane, Y. Tang, *J. Membr. Sci.* **2015**, *499*, 201.

[60] S. Zhao, Z. Liao, A. Fane, J. Li, C. Tang, C. Zheng, J. Lin, L. Kong, *Desalination* **2021**, *499*, 114857.

[61] X. Li, C. Liu, W. Yin, H. Chong, R. Wang, *J. Membr. Sci.* **2019**, *584*, 309.

[62] G. S. Goon, O. Labban, Z. H. Foo, X. Zhao, J. H. Lienhard, *J. Membr. Sci.* **2021**, *626*, 119169.

[63] F. Ricceri, M. Giagnorio, K. R. Zodrow, A. Tiraferri, *J. Membr. Sci.* **2021**, *619*, 376.

[64] V. N. Francis, J. Y. Chong, G. Yang, L. Che, R. Wang, *Chem. Eng. J.* **2023**, *452*, 139333.

[65] B. Sutariya, S. Karan, *Sep. Purif. Technol.* **2022**, *293*, 1383.

[66] L. F. Villalobos, K. E. Pataroque, W. Pan, T. Cao, M. Kaneda, C. Violet, C. L. Ritt, E. M. V. Hoek, M. Elimelech, *J. Membr. Sci. Lett.* **2023**, *3*, 100048.

[67] J. Wang, R. S. Kingsbury, L. A. Perry, O. Coronell, *Adv. Environ. Sci. Technol.* **2017**, *51*, 2295.

[68] R. Wang, R. He, T. He, M. Elimelech, S. Lin, *Nat. Water* **2023**, *1*, 291.

[69] Y. Zhang, L. Wang, W. Sun, Y. Hu, H. Tang, *J. Industr. Eng. Chem.* **2020**, *81*, 7.

[70] H. Fan, N. Y. Yip, *J. Membr. Sci.* **2019**, *573*, 668.

[71] H. B. Park, J. Kamcev, L. M. Robeson, M. Elimelech, B. D. Freeman, *Science* **2017**, *356*, 1138.

[72] Z. Kargozarfard, A. Haghtalab, S. Ayatollahi, M. H. Badizad, *Ind. Eng. Chem. Res.* **2020**, *59*, 22258.

[73] X. Tang, P. H. Koenig, R. G. Larson, *J. Phys. Chem. B* **2014**, *118*, 3864.

[74] D. Hou, Y. Jia, J. Yu, P. Wang, Q. Liu, *J. Phys. Chem. C* **2018**, *122*, 28021.

[75] O. Coronell, M. I. González, B. J. Mariñas, D. G. Cahill, *Adv. Environ. Sci. Technol.* **2010**, *44*, 6808.

[76] J. C. Phillips, R. Braun, W. Wang, J. Gumbart, E. Tajkhorshid, E. Villa, C. Chipot, R. D. Skeel, L. Kale, K. Schulten, *J. Comput. Chem.* **2005**, *26*, 1781.

[77] Z. Zha, T. Li, I. Hussein, Y. Wang, S. Zhao, *J. Membr. Sci.* **2024**, *695*, 122484.

[78] S.-L. Gao, Z.-X. Qin, B.-F. Wang, J. Huang, Z.-L. Xu, Y.-J. Tang, *Desalination* **2024**, *572*, 117142.

[79] Y. D. Ahdab, G. Schücking, D. Rehman, J. H. Lienhard, *Appl. Energy* **2021**, *301*, 117425.

[80] C. F. Baspineiro, J. Franco, V. Flexer, *Sci. Total Environ.* **2020**, *720*, 137523.

[81] Z. Wang, D. Feng, Y. Chen, D. He, M. Elimelech, *Environ. Sci. Technol.* **2021**, *55*, 10714.

[82] J. Zhang, *WIREs Comput. Stat.* **2021**, *13*, e1539.

[83] S. Liu, S. Keten, R. M. Lueptow, *J. Membr. Sci.* **2023**, *678*, 121630.

[84] S. Liu, S. Ganti-Agrawal, S. Keten, R. M. Lueptow, *J. Membr. Sci.* **2022**, *644*, 120057.

[85] M. Ding, A. Szymczyk, A. Ghoufi, *Desalination* **2015**, *368*, 76.

[86] K. Leung, S. B. Rempe, *J. Comput. Theor. Nanosci.* **2009**, *6*, 1948.

[87] Y. Luo, E. Harder, R. S. Faibish, B. Roux, *J. Membr. Sci.* **2011**, *384*, 1.

[88] S. Liu, Z. H. Foo, J. H. Lienhard, S. Keten, R. M. Lueptow, *In Preparation* **2024**.

[89] J. Wang, R. M. Wolf, J. W. Caldwell, P. A. Kollman, D. A. Case, *J. Comput. Chem.* **2004**, *25*, 1157.

[90] A. Jakalian, D. B. Jack, C. I. Bayly, *J. Comput. Chem.* **2002**, *23*, 1623.

[91] J. Wang, W. Wang, P. A. Kollman, D. A. Case, *J. Mol. Graph.* **2006**, *25*, 247.

[92] T. T. Duignan, X. S. Zhao, *Phys. Chem. Chem. Phys.* **2020**, *22*, 25126.

[93] R. Epsztein, E. Shaulsky, N. Dizge, D. M. Warsinger, M. Elimelech, *Adv. Environ. Sci. Technol.* **2018**, *52*, 4108.

[94] A. Yaroshchuk, M. L. Bruening, E. Zholkovskiy, *Adv. Colloid Interface Sci.* **2019**, *268*, 39.

[95] J. Kim, K. Park, S. Hong, *Desalination* **2020**, *492*, 114645.